J Adv Ceram

Research Article

A nacre formation-inspired dynamic self-generating barrier for environmental deposit-resistant thermal barrier coatings

Yao-Xu Zan, Lu Huang, Wei-Zheng Gu, Peng-Shuai Yue, Lin Dong, Mei-Jun Liu✉, Guan-Jun Yang

Cite this article: Zan Y-X, Huang L, Gu W-Z, et al. *J Adv Ceram* 2026, **15**(1): 9221218. https://doi.org/10.26599/JAC.2025.9221218

ABSTRACT: To address the challenge of corrosion in thermal barrier coatings (TBCs) by low-calcium-silica-ratio, impurity-containing environmental deposits (CMAS-E) in advanced aeroengines, this study, inspired by the adaptive defense mechanism of nacre formation, designs a $Zr_{3/7}Y_{8/21}Yb_{2/21}Gd_{2/21}O_{12/7}$ (YYbGdZO) coating with a biomimetic "dynamic self-response" functionality. The coating demonstrated high durability at 1400 °C and remained stable for 100 h, with a reaction layer of only 18.8±1.5 μm and no buckling failure mode. The origin of this resistance lies in the high reactivity of the YYbGdZO layer, which, upon contact with the molten "stimulus", forms a multifunctional dynamic self-generating barrier *in situ* via a rapid interfacial reaction. This barrier consists of an outer continuous rare-earth (RE) silicate layer for physical blockade and an inner apatite/fluorite composite that is structurally analogous to a nacre-like "brick-and-mortar" architecture, which synergistically achieves chemical passivation and suppresses ion diffusion. This efficient sealing response transforms the entire corrosion process from an initial stage of rapid infiltration and reaction into a slow, diffusion-controlled stage governed by this dense barrier, which follows a parabolic law. The biomimetic "dynamic self-response" mechanism elucidated in this work provides an effective new strategy for developing TBCs with long-term durability and high reliability against environmental deposit corrosion.

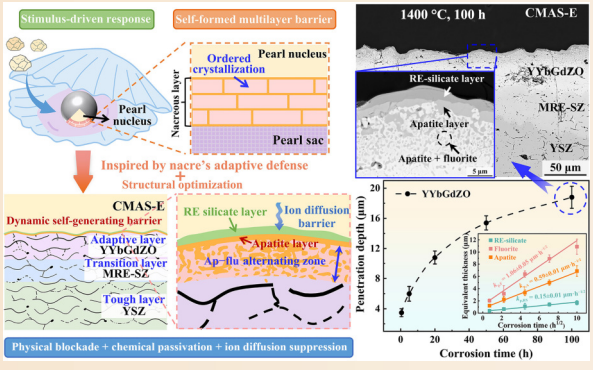

KEYWORDS: multicomponent rare-earth (MRE); buckling; biomimetic multilayer coating; environmental deposit resistance; defense barrier

1 Introduction

Thermal barrier coatings (TBCs) are applied to hot-section components of power equipment, such as aeroengines, to provide thermal protection against gas temperatures exceeding 1300 °C and to extend the service life of substrate alloys [1–4]. The current mainstream TBC ceramic layer is typically composed of 7–8 wt% Y_2O_3-stabilized ZrO_2 (YSZ). However, in service environments, engines often ingest sand or volcanic ash, which melts at high temperatures to form a silicate melt predominantly composed of CaO–MgO–Al_2O_3–SiO_2, known as CMAS deposits [5]. Once deposited on the TBC surface, the molten CMAS rapidly infiltrates the pores of the coating and microcracks via capillary action. During infiltration, the molten CMAS engages in complex chemical reactions with the coating material. This process dissolves the rare-earth (RE) stabilizer and induces detrimental phase transformations upon cooling, degrading the coating's phase composition and microstructure, significantly impairing its thermal insulation performance, reducing its strain tolerance, and ultimately accelerating coating failure [6]. Consequently, CMAS corrosion has become a severe problem that threatens TBC lifetime and has attracted significant attention from both the academic and engineering communities.

To address the challenge of CMAS corrosion, a series of strategies have been proposed in recent years to improve the CMAS resistance of coatings. One approach focuses on optimizing the coating microstructure to reduce infiltration pathways, for example, by densifying the coating surface via laser remelting [7,8] or by depositing a dense protective layer on the YSZ surface to block CMAS ingress. For example, Zhang *et al.* [9] synthesized a dense α-Al_2O_3 layer *in situ* on a 7YSZ TBC surface, which effectively hindered CMAS penetration and formed high-melting-point phases upon reaction with CMAS, thereby significantly enhancing the corrosion resistance of the coating. A second approach involves surface engineering, where the macroscopic morphology and chemical properties of the coating are modified to mitigate CMAS infiltration. Zhuo *et al.* [10] developed a synergistic strategy by combining a laser-fabricated, biomimetic superhydrophobic surface with an *in situ* synthesized Al-modified protective layer. This approach significantly increased

State Key Laboratory for Mechanical Behavior of Materials, School of Materials Science and Engineering, Xi'an Jiaotong University, Xi'an 710049, China.

✉ Corresponding author. E-mail: liumjun@xjtu.edu.cn

Received: September 22, 2025; Revised: October 31, 2025; Accepted: November 25, 2025

the contact angle of the molten CMAS during *in situ* testing at 1230 °C, effectively suppressing wetting, spreading, and infiltration, thus markedly improving the resistance of the coating to CMAS corrosion. Another approach is the development of novel coating materials with intrinsic resistance to CMAS corrosion, such as multi-RE stabilized zirconia [11–13], RE zirconates ($RE_2Zr_2O_7$) [14–16], phosphates [17,18], and high-entropy ceramics [19–21]. Typically, $RE_2Zr_2O_7$, as candidate materials to replace YSZ, offer lower thermal conductivity and improved phase stability. Furthermore, they readily react with CMAS at high temperatures to form stable apatite-structured phases, creating a dense, impermeable sealing layer at the interface that effectively prevents further CMAS penetration. For example, Zhang *et al.* [16] achieved a significant improvement in CMAS infiltration resistance by controlling the La content in nonstoichiometric lanthanum zirconate TBCs prepared by plasma spraying; a higher La content promoted the formation of a La-apatite sealing layer, effectively inhibiting the penetration and corrosion of molten CMAS. Additionally, codoping with multiple RE elements has been employed to enhance the high-temperature properties of YSZ. Multicomponent systems, such as Gd–Yb–Y codoped zirconia, can form defect clusters within the crystal lattice, thereby reducing the thermal conductivity and enhancing the phase stability [22,23]. However, their resistance to CMAS corrosion remains controversial: some studies report that these coatings can react with the melt at high temperatures to form protective phases, significantly slowing infiltration and reactions [12,13], whereas other studies indicate deeper penetration and earlier phase transformation under similar conditions [24]. This suggests that the anti-CMAS efficacy of Gd–Yb–Y-stabilized zirconia coatings is dependent on factors such as service temperature and melt composition, and their intrinsic corrosion and protection mechanisms require further elucidation. Overall, while these methods can delay CMAS attack to some extent, they are often associated with challenges such as complex fabrication processes, increased thermal expansion mismatch, or degraded mechanical properties, which limit their application scope and service reliability. Furthermore, a substantial body of existing research has utilized CMAS systems based on widely adopted, standardized compositions with high Ca/Si ratios (e.g., 33CaO–9MgO–13$AlO_{1.5}$–45SiO_2, mol%). However, real-world service deposits (such as volcanic ash and desert dust) exhibit significantly different chemical characteristics; not only do the Ca/Si ratio vary with geographical origin, but they also frequently contain impurity elements such as Fe, Ti, K, and Na [25]. This compositional variance fundamentally alters the physicochemical properties of the melt, rendering its corrosive behavior and failure mechanisms far more complex and severe than traditionally understood [26–29]. Wu *et al.* [30] demonstrated that within the same melt system, as the Ca content decreases from 33 to 19 mol%, the driving force for RE ions to precipitate as apatite is significantly weakened, leading to a substantial reduction in the amount of protective apatite formed within a short duration. Therefore, corrosion conditions involving environmental deposits rich in impurities such as K, Na, Fe, and Ti and featuring a low Ca/Si ratio (termed CMAS-E in this work), many of which rely on apatite formation, may prove ineffective. This not only reveals a critical gap between prevailing research models and actual service conditions but also creates an urgent need for a new generation of coating design philosophies capable of maintaining robust protection under these more severe and realistic conditions.

Accordingly, this paper proposes a design concept for a biomimetic coating with a dynamic interface response intended to significantly enhance the corrosion resistance of TBCs in severe CMAS-E environments. This design is inspired by the encapsulation protection mechanism of nacre, whereby mollusks protect themselves from foreign intruders, such as sand grains, by progressively encapsulating them with secreted layers. Analogously, this study, which builds upon previous designs [31,32], employs a biomimetic multilayer architecture to achieve synergistic protection through functionally distinct layers: A reactive layer enriched with active RE components (Y/Yb/Gd) preferentially reacts with environmental deposits at high temperatures to form a dense barrier layer *in situ*, thereby actively suppressing melt infiltration; a transition layer provides both thermal insulation and stress buffering, effectively mitigating interfacial mismatch and enhancing structural stability; and a tough, YSZ-based layer, which, with its excellent toughness and thermal compatibility, provides overall support and service reliability. The core of this design is the *in situ* formation of a dual-phase composite barrier by the top ceramic layer during the corrosion process, which enables the coating to self-assemble into a protective "wall" at the site of attack, achieving the dual defensive effects of physical blockade and chemical passivation [31]. Through this multilayer synergistic mechanism of "active capture, thermal buffering, and mechanical support", the coating can realize a dynamic, response-based defense against corrosion in CMAS-E service environments.

To address the formidable challenge posed by low-Ca/Si-ratio CMAS-E corrosion, this work, which is grounded in the aforementioned biomimetic multilayer TBC design, introduces a dynamic interface optimization strategy inspired by the nacre formation process. This strategy uses multiple principal RE elements to synergistically regulate precipitated phases, aiming to construct a novel defense system distinct from traditional apatite-based protection mechanisms. This study systematically investigated the performance and underlying mechanisms of a coating under CMAS-E corrosion conditions, coupled with an in-depth analysis of its microstructural evolution. This study first determines the influence of the surface morphology of the novel $Zr_{3/7}Y_{8/21}Yb_{2/21}Gd_{2/21}O_{12/7}$ coating on the wetting behavior and interfacial evolution of CMAS-E. Subsequently, high-temperature corrosion experiments at 1400 °C are used to analyze the phase composition and microstructural evolution of the coating at various stages of corrosion. This work culminates in an in-depth exploration of the multistage, *in situ* formation of a protective barrier, revealing how the synergy between multicomponent chemistry and microstructure-guided preferential nucleation results in a multifunctional composite defense system. This research not only validates the feasibility of the biomimetic design but also provides a novel design concept for developing high-temperature coatings with resistance to environmental deposit corrosion.

2 Experimental

2.1 Materials preparation and coating deposition

2.1.1 *Feedstock powders*

Within the ceramic layers, the tough and transition layers were fabricated using commercial YSZ (Metco 204B-NS) and multicomponent rare-earth stabilized zirconia (MRE-SZ) powders as feedstocks, respectively. The top ceramic layer was fabricated via laboratory-synthesized $Zr_{3/7}Y_{8/21}Yb_{2/21}Gd_{2/21}O_{12/7}$ (hereafter referred to as YYbGdZO) powder. This powder was synthesized via a solid-state reaction method, agglomerated, and granulated by

spray drying, and subsequently posttreated by sintering to obtain spherical particles. The information for the feedstock powders is detailed in Table 1. The YSZ, MRE-SZ, and YYbGdZO powders were sieved through 200- and 500-mesh screens. The surface morphologies and particle size distributions of the powders are presented in Fig. 1. All three powders exhibited a near-spherical morphology overall but differed in surface roughness. The YSZ particles (Fig. 1(a)) had relatively smooth and dense surfaces, whereas the MRE-SZ powders (Fig. 1(b)) displayed localized surface roughening. The YYbGdZO powders (Fig. 1(c)) were generally spherical, but some particles showed surface pits or collapses, a common feature of ceramic powders produced by spray granulation and sintering. The particle size distributions were measured via a laser diffraction particle size analyzer (Mastersizer 3000, Malvern Panalytical, UK). The distribution curves (Figs. 1(d)–1(f)) show that the median particle sizes (d_{50}) of the YSZ, MRE-SZ, and YYbGdZO powders were 58.9, 54.7, and 50.1 μm, respectively, indicating that all three powders have similar particle size ranges, making them suitable for the subsequent thermal spray process.

2.1.2 *Environmental deposits*

ISO 12103-1 A4 environmental sand dust was used as the high-temperature environmental deposit corrosion source. Its morphology and particle size distribution are shown in Fig. 2. Scanning electron microscopy (SEM) imaging (Fig. 2(a)) revealed that the powder primarily exhibited an irregular, blocky morphology. The results of the particle size analysis (Fig. 2(b)) indicate that d_{50} is approximately 3.11 μm. The chemical composition of this dust, previously determined by our laboratory via X-ray fluorescence (XRF) analysis [31], is presented in Table 2. Compared with the standard CMAS systems reported in [33–35], this environmental dust contains additional impurity elements, such as potassium, sodium, iron, and titanium. Furthermore, the mass percentages of CaO, MgO, and Al_2O_3 are significantly lower. To distinguish it from standard CMAS systems, the environmental deposit containing Na, K, Fe, and Ti impurities is designated CMAS-E in this study.

2.1.3 *Coating preparation*

304 stainless steel plates with dimensions of 20 mm × 80 mm × 3 mm were used as the substrate material. Ceramic coatings (YSZ, MRE-SZ, and YYbGdZO) were prepared via the APS technique, and the deposition parameters are listed in Table 3. In accordance with the design, three types of coatings were fabricated, each with a total nominal thickness of 180±10 μm: a single-layer YYbGdZO coating, a double-layer MRE-SZ/YSZ coating (~75/~105 μm), and a multilayer YYbGdZO/MRE-SZ/YSZ coating (~40/~40/~100 μm). The as-sprayed coatings were cut into 10 mm × 10 mm × 3 mm rectangular samples via a precision diamond wire saw. The samples were subsequently immersed in a 38 wt% hydrochloric acid solution. Once the metallic substrate was substantially dissolved and the ceramic coating detached automatically, the coating was promptly removed, thoroughly rinsed with deionized water and ethanol, and then dried to obtain free-standing coating samples.

2.2 Wetting and spreading behavior of environmental deposits

To evaluate the wetting behavior of the molten environmental deposits on the surfaces of the APS-fabricated coatings, high-temperature contact angle measurements were conducted. Initially, the CMAS-E powders were pressed into a pellet and then machined into a 2 mm cubic sample, which was subsequently

Table 1 Ceramic powder materials for atmospheric plasma spraying (APS) coatings

Powder	Chemical composition	Granularity (μm)	Morphology	Supplier
YSZ	ZrO_2–$8Y_2O_3$	30–80	Spheroidal	Oerlikon Metco, Switzerland
MRE-SZ	ZrO_2–$10Y_2O_3$–$5Yb_2O_3$–$5Gd_2O_3$	30–90	Spheroidal	Xi'an Aerospace Composite Materials Research Institute, China
YYbGdZO	$Zr_{3/7}Y_{8/21}Yb_{2/21}Gd_{2/21}O_{12/7}$	20–100	Spheroidal	Laboratory-synthesized powder, China

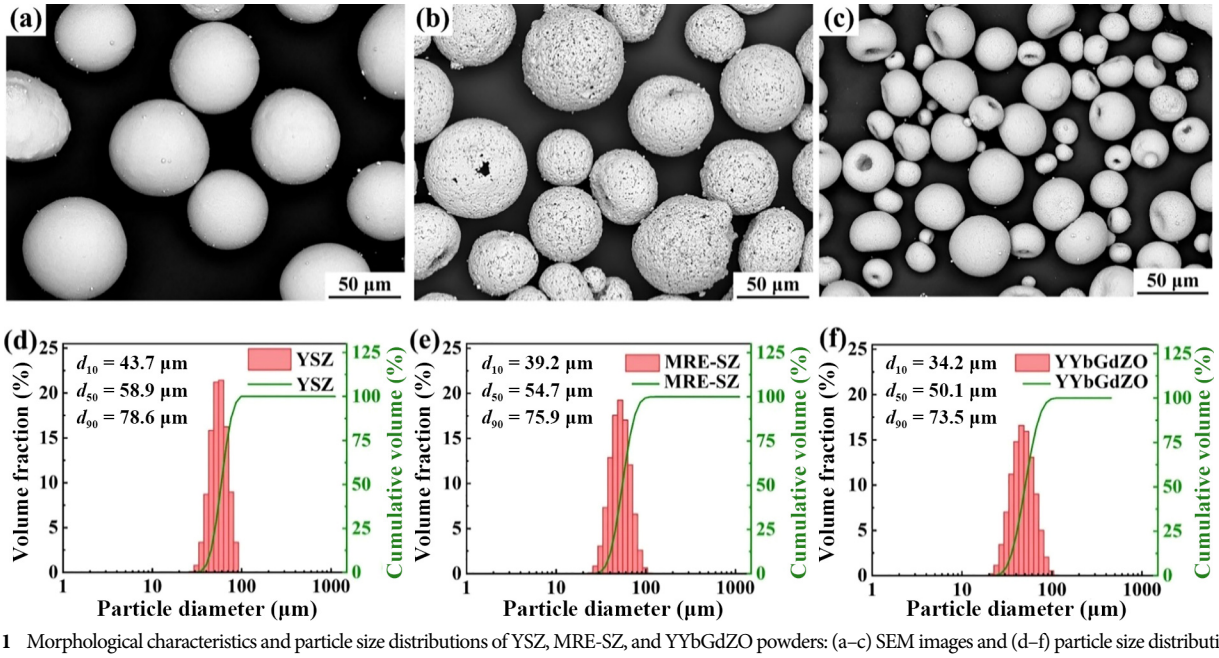

Fig. 1 Morphological characteristics and particle size distributions of YSZ, MRE-SZ, and YYbGdZO powders: (a–c) SEM images and (d–f) particle size distributions.

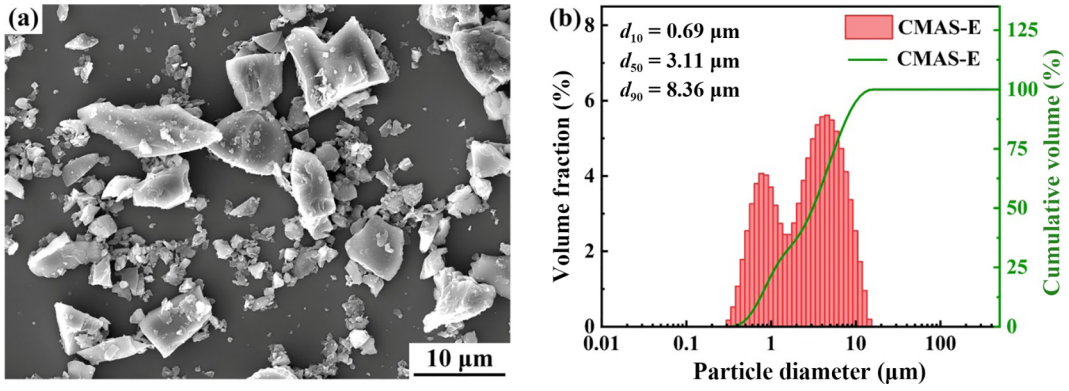

Fig. 2 Morphology and particle size distribution of environmental deposits (CMAS-E): (a) SEM image and (b) particle size distribution curve.

Table 2 Chemical composition of ISO 12103-1 A4 test sand dust (CMAS-E) (Unit: wt%)

Oxide	CaO	MgO	Al_2O_3	SiO_2	Na_2O	K_2O	Fe_2O_3	TiO_2
Weight	3.17	1.09	8.52	79.86	1.71	3.27	2.09	0.29

Table 3 Parameters of the atmospheric plasma-sprayed ceramic coating

Parameter	YSZ	MRE-SZ	YYbGdZO
Arc power (kW)	39	42	42
Plasma gas (Ar) flow (SLM)	50	50	50
Plasma gas (H_2) flow (SLM)	6	8.0	8.0
Plasma gas (N_2) flow (SLM)	5.0	5.0	5.0
Torch traverse speed (mm/s)	800	800	800
Spray distance (mm)	90	90	90
Powder feed rate (r/min)	3.0	3.0	3.0

Note: SLM stands for standard liters per minute, which is the unit of gas flow rate under standard conditions.

placed on the coating surface. Two types of single-layer YYbGdZO free-standing coatings with different surface states were used as substrates: one featuring an as-sprayed rough surface and the other featuring a ground and polished smooth surface. The samples were heated to 1000 °C at a rate of 10 °C/min and subsequently to 1400 °C at 5 °C/min, during which the spreading and infiltration behavior of the molten CMAS-E was monitored. Throughout the entire process, images were captured at 5 s intervals to document the evolution of the contact angle.

2.3 Corrosion behavior tests

To investigate the reaction products between the TBC materials and the melt, a powder-compact method was employed to study their high-temperature interactions. The fabricated free-standing MRE-SZ and YYbGdZO coatings were first crushed in an agate mortar. This "preparation-then-crushing" approach was intentionally chosen to ensure that the starting material for phase analysis accurately reflected the phase composition of the as-sprayed coating. Rapid melting and solidification during the plasma spraying process can induce the formation of metastable phases that differ from those of the original feedstock powder. Therefore, the use of powder derived from the actual coating ensures that the results from macroscopic phase analysis via X-ray diffraction (XRD) are directly comparable to those from microstructural corrosion analysis of the coating samples via SEM. The resulting powders were then mixed with CMAS-E powders at a mass ratio of 2 : 1 and subsequently ball-milled in an ethanol medium using zirconia balls (600 r/min, 3 h, ball-to-powder ratio of 3 : 1). The resulting slurry was vacuum-dried and passed through a 500-mesh sieve to obtain a homogeneously mixed powder. The mixed powder was then uniaxially pressed into pellets at 150 MPa. These as-pressed pellets were placed in a box furnace, heated from 1000 to 1400 °C at a rate of 5 °C/min, and held for 0.5, 5, and 20 h to obtain bulk samples of the reacted CMAS-E and TBC materials (MRE-SZ and YYbGdZO) for phase analysis of the reaction products.

A controlled slurry deposition technique was used to deposit CMAS-E powders onto the free-standing coating surfaces to investigate the microstructural evolution of the coatings at 1400 °C. Specifically, the CMAS-E powders were ultrasonically dispersed in ethanol to form a uniform slurry, which were then evenly deposited onto the 10 mm × 10 mm surfaces of the free-standing TBCs at a controlled density of 30±2 mg/cm^2. After drying, the coated samples were subjected to isothermal heat exposure in a high-temperature furnace in ambient air. A programmed heating schedule was used: the heating rate was 10 °C/min up to 1000 °C, and the heating rate was 5 °C/min from 1000 to 1400 °C. After exposure for various durations (0.5, 5, 20, 50, and 100 h), the samples were cooled to 1000 °C at a rate of 5 °C/min and then furnace-cooled to room temperature.

2.4 Characterizations

The surface roughness and three-dimensional (3D) surface morphology of the coatings were measured via a 3D laser scanning confocal microscope (OLS5000, OLYMPUS, Japan). The surface and cross-sectional microstructures of the samples were observed by an SEM (MIRA 3 LMH, Tescan, Switzerland) in both secondary electron (SE) and backscattered electron (BSE) modes. The elemental composition and distribution were analyzed via an energy-dispersive spectrometer (EDS; AZTEC, Oxford

Instruments, UK) coupled with SEM. The thickness of the reaction layer was determined via quantitative image analysis. Specifically, the area of the reaction layer in the cross-sectional images was measured via ImageJ software and then divided by the projected length of the reaction interface to obtain an equivalent thickness. The equivalent thickness of each phase within the reaction layer was measured from BSE images acquired at 10,000× magnification. These images were first binarized to segment the different phase regions, after which the area fraction of each phase was calculated via ImageJ and divided by the projected length of the reaction interface to determine its corresponding equivalent thickness. To ensure the representativeness and accuracy of the results, all the quantitative data derived from the cross-sectional images, including the total reaction zone depth and the equivalent thickness of each phase, were obtained by measuring and averaging the values from at least five different regions for each sample. Phase analysis of the bulk samples, comprising mixtures of CMAS-E and TBC materials (MRE-SZ and YYbGdZO) reacted at 1400 °C for different durations, was conducted via an XRD (D8 Advance 3.0, Bruker). Scans were performed over a 2θ range of 10°–90° with a step size of 0.02° and dwell time of 0.1 s per step, corresponding to a scan speed of 12 (°)/min. The cross-sectional elemental distributions of the biomimetic multilayer coating and its YYbGdZO top layer after 20 h of corrosion at 1400 °C were characterized via an electron probe microanalyzer (EPMA; JXA-HP200F, JEOL, Japan) under optimized analytical conditions (accelerating voltage of 15 kV and beam current of 50 nA). Elemental mapping was performed via the instrument's built-in standard calibration parameters. The diffraction crystals and corresponding characteristic X-rays used for each element were as follows: Si Kα-TAP, Na Kα-TAP, Ca Kα-PETJ, K Kα-PETH, Zr Lα-PETH, Mg Kα-TAP, Ti Kα-PETJ, Fe Kα-LIFH, Gd Lα-LIFH, Al Kα-TAP, Yb Lα-LIF, and Y Lα-PETH. Specifically, PET, TAP, and PETH refer to pentaerythritol, thallium acid phthalate, and high-resolution pentaerythritol analyzing crystals, respectively. The mechanical properties of each layer of the coating were characterized via a commercial nanoindenter (TI950, Hysitron TriboIndenter, USA) equipped with a Berkovich diamond indenter. To minimize the influence of surface roughness, all tests were performed on polished cross-sections of the coatings. The tests were conducted in load-controlled mode with a maximum load of 8000 μN. Both the loading and unloading cycles were set to 5 s (corresponding to a rate of 1600 μN/s), and a holding time of 2 s was applied at the peak load to minimize creep effects. To ensure the reliability of the data, indentations were performed in no fewer than 5 different regions for each sample layer (YSZ, MRE-SZ, and YYbGdZO), and the average values and standard deviations were calculated.

3 Results and discussion

3.1 Effect of surface roughness on the spreading and wetting behavior of CMAS-E on YYbGdZO coating surfaces

To investigate the influence of surface roughness on the spreading and wetting characteristics of CMAS-E, a comparative study was conducted using YYbGdZO coatings with two different surfaces: an as-sprayed surface (average surface roughness (S_a) ≈ 6.75 μm) and a ground and polished surface (S_a ≈ 0.5 μm). The 3D surface morphologies of these materials are shown in Figs. 3(a) and 3(c), respectively. The as-sprayed surface clearly exhibited distinct peaks and valleys, whereas the polishing treatment significantly reduced the surface undulations, resulting in a much flatter topography. The temperature-dependent evolution of the CMAS-E contact angle on both surfaces is presented in Figs. 3(b) and 3(d). At room temperature, a CMAS-E pellet was placed on each coating surface. Upon heating to 1300 °C, the CMAS-E pellet began to melt, exhibiting a contact angle greater than 100° on both surfaces. As the temperature increased to 1350 °C, the contact angle decreased significantly from an initial value of ~107° to ~102° on the rough surface and then to ~88° on the smooth surface, indicating that the CMAS-E had started to melt and spread. With a further increase to 1375 °C, the contact angles on the rough and smooth surfaces decreased to ~80° and ~60°, respectively, revealing a more pronounced wetting effect of the molten CMAS-E on the polished surface. By 1400 °C, the contact angle on the rough surface remained between ~58° and ~66°, whereas on the smooth surface, it rapidly decreased to ~37°, demonstrating that CMAS-E achieved a much greater spreading capability on the flatter surface.

These results indicate that the surface roughness of the coating has a significant effect on the spreading and wetting behavior of CMAS-E. The numerous peaks and valleys on the rough surface initially retard the spreading of the melt, leading to a relatively slow decrease in the contact angle. In contrast, the smooth surface facilitates the spreading and infiltration of the molten CMAS-E, resulting in more pronounced wettability at high temperatures. This difference demonstrates that by controlling the surface morphology of the coating, the wetting kinetics of molten CMAS can be effectively influenced, which in turn has a potential impact on the resistance of the coating to CMAS corrosion.

3.2 Microstructural response of YYbGdZO coating surfaces and cross-sections under CMAS-E attack

Figure 4 shows the surface microstructural features of the as-sprayed and polished YYbGdZO coatings after reacting with molten CMAS-E at 1400 °C for 30 min. For the as-sprayed coating (Figs. 4(a)–4(c)), the rough surface, characterized by numerous peaks, valleys, and pores, significantly influenced the wetting and spreading behavior of the molten CMAS-E. The melt wetted the coating surface and infiltrated along the pore network, forming a reaction-affected zone. At the edge of the wetted region, a reaction between the melt and the coating was observed, with the reaction products gradually filling some of the pores. This edge region was selected for detailed analysis because it represents the leading front of the melt-coating interaction, where a thinner melt layer is most conducive to clearly observing the interfacial reaction. According to EDS analysis, point Y2 contains both RE silicate and fluorite phases, likely resulting from signal overlap between the reaction products, residual melt, and underlying coating. Although the overall roughness and local peak-valley structures of the as-sprayed surface somewhat hindered the spread of the melt, the abundant pores still served as infiltration channels. Nevertheless, during the wetting and spreading process, the YYbGdZO coating underwent interfacial reactions that impeded further penetration. In contrast, the polished coating surface was flat, with almost no distinct peaks or valleys, providing a more uniform environment for the growth of the reaction products. As shown in Fig. 4(f) and confirmed by EDS analysis (Fig. 4(h) and Table 4), the reaction between CMAS-E and the flat surface resulted in the formation of a continuous reaction product layer, which included plate-like silicate phases (Product 1) and rod-bundle apatite phases (Product 2). The nucleation and growth of these reaction products proceeded smoothly on the flat surface, and the resulting layer effectively blocked further melt infiltration.

A comparison of the microstructural responses of the as-

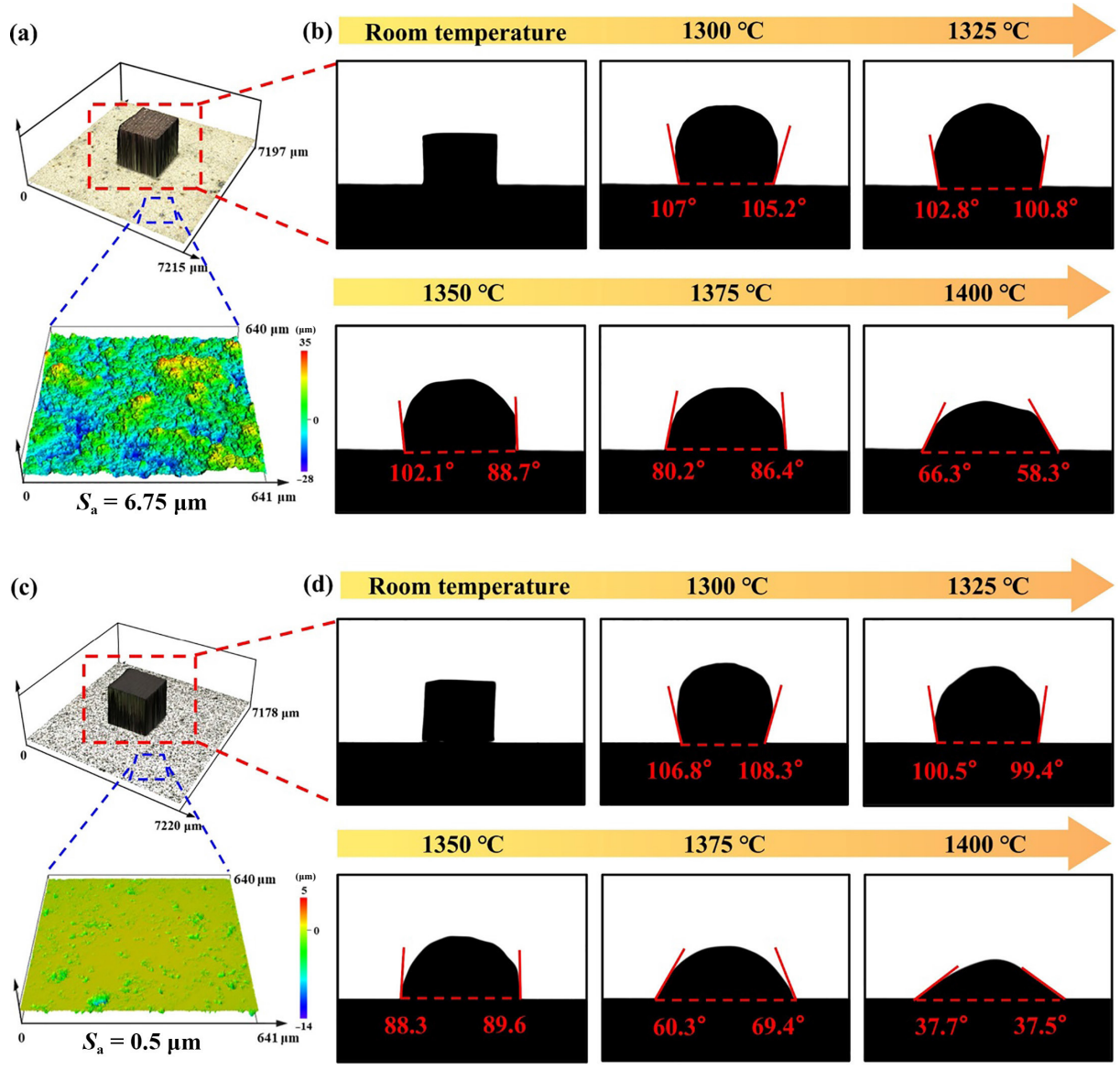

Fig. 3 Surface morphology of YYbGdZO coatings with different roughnesses and evolution of contact angle of molten CMAS-E during heating: (a, c) 3D surface morphology of as-sprayed and polished surfaces; (b, d) variation in contact angle of CMAS-E block from room temperature to 1400 °C.

sprayed and polished coatings after reacting with CMAS-E reveals that surface roughness significantly affects the wetting, spreading, and reaction processes of the melt. On the rough surface, the numerous protrusions and peak-valley structures restricted uniform spreading, resulting in a slower spreading rate for the melt. Conversely, on the flat, polished surface, the lower roughness allowed for a faster spreading rate, as the surface topography offered less resistance, enabling the melt to spread and react with the coating material more rapidly.

Although the melt spread more easily on the low-roughness surface, the YYbGdZO coating, through its unique rapid crystallization-reaction mechanism, was able to quickly form a stable reaction product layer during the spreading process, effectively sealing the infiltration pathways. This crystallization reaction enabled the coating to react promptly with the infiltrating melt and precipitate reaction products, thereby preventing further penetration into the interior of the coating and significantly enhancing its corrosion resistance to CMAS-E. This result demonstrates that even under conditions of rapid melt spreading, the YYbGdZO coating can effectively resist melt infiltration and corrosion via its rapid reaction-crystallization mechanism, forming a dense protective barrier that maintains the stability and durability of the coating.

To investigate the influence of surface roughness on the interaction and corrosion behavior of molten CMAS-E with the YYbGdZO coating, the cross-sectional microstructures of both coating types were characterized after 30 min of thermal corrosion at 1400 °C. Figure 5 displays the cross-sectional morphology of the as-sprayed YYbGdZO coating. The macroscopic view (Fig. 5(a)) shows that the solidified CMAS-E melt covers the coating surface, forming an interface with an irregular profile that conforms to the original rough topography. No significant large-scale penetration was observed. At the edge of the spread melt (Figs. 5(b) and 5(c)), a thin, continuous, and dense reaction product layer is observed to have formed between the CMAS-E and the YYbGdZO coating. This reaction layer closely adheres to the peak-and-valley topography of the coating surface, effectively isolating the overlying CMAS melt from the underlying coating substrate. In the central region of the melt-coating interface (Figs. 5(d) and 5(e)), where the melt concentration was highest, the corrosion

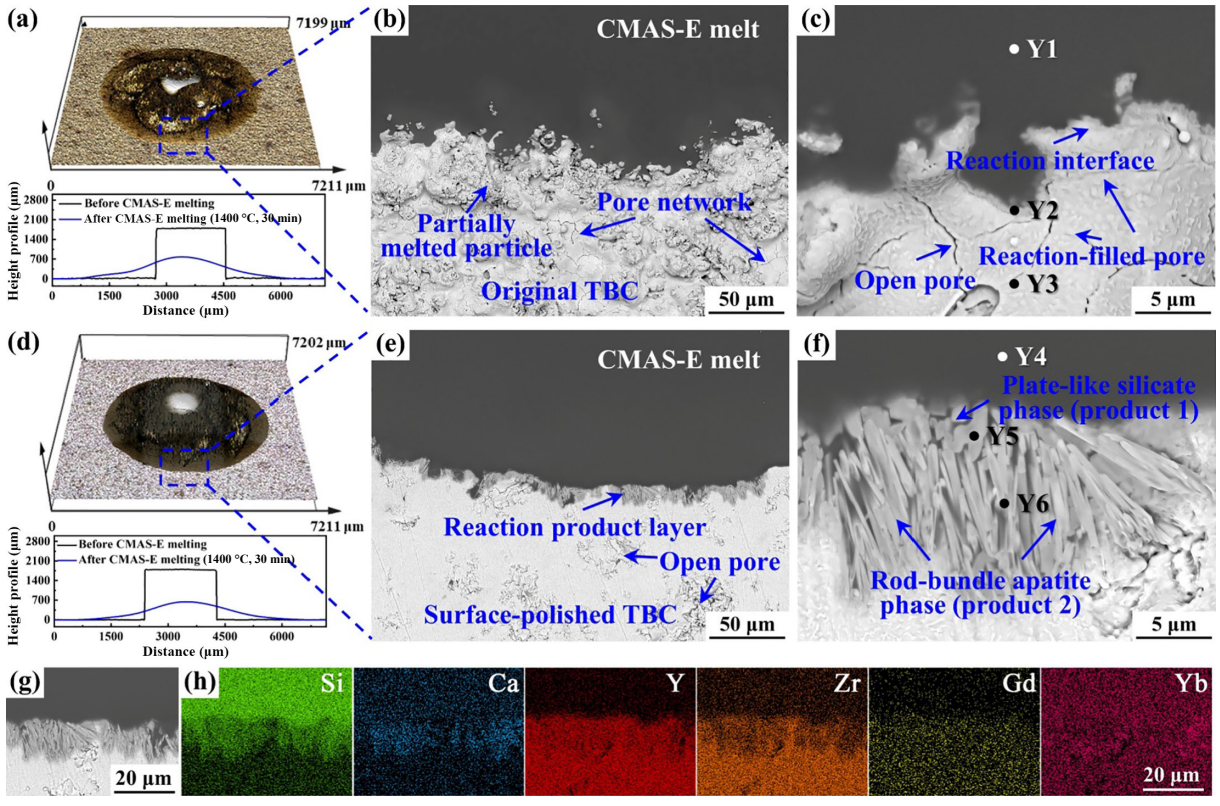

Fig. 4 3D surface morphology and microstructural features of as-sprayed and polished YYbGdZO coatings after reaction with molten CMAS-E at 1400 °C for 30 min: (a, d) surface morphology and height profile variations; (b, e) microstructures at wetting boundary of CMAS-E melt on surface; (c, f) high-magnification images showing reaction interface and pore-filling products; (g, h) surface morphology of polished coating and corresponding elemental distribution maps.

Table 4 Elemental compositions (at%) of points indicated in Figs. 4(c) and 4(f)

Sample		Composition (at%)												Phase
		Si	Ca	Na	Al	Mg	K	Fe	Y	Yb	Gd	Zr	O	
As-sprayed coating	Y1	22.5	1.1	1.3	4.4	0.4	0.9	0.1	—	—	—	—	69.4	Melt
	Y2	4.5	—	—	—	—	—	—	10.7	2.4	2.0	7.9	72.5	Silicate + fluorite
	Y3	—	—	—	—	—	—	—	17.0	3.3	3.1	14.5	62.2	Fluorite
Surface-polished coating	Y4	29.1	1.0	1.6	4.3	—	1.2	—	—	—	—	—	62.8	Melt
	Y5	17.0	—	—	—	—	—	—	11.1	2.3	2.2	—	67.4	Silicate
	Y6	12.9	3.1	—	—	—	—	—	13.7	0.7	3.6		66.0	Apatite

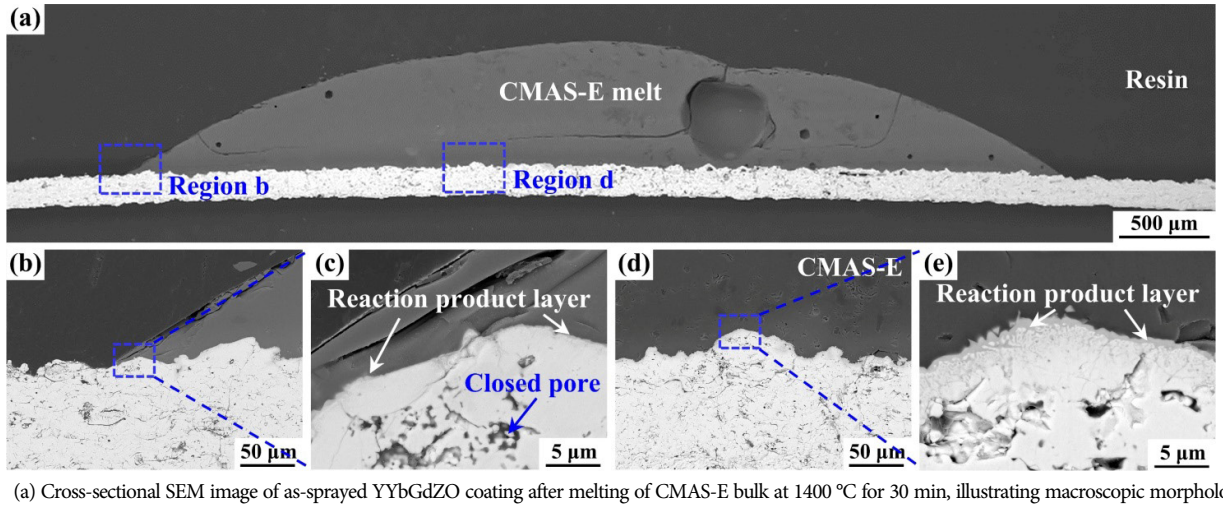

Fig. 5 (a) Cross-sectional SEM image of as-sprayed YYbGdZO coating after melting of CMAS-E bulk at 1400 °C for 30 min, illustrating macroscopic morphology of melt/coating interface. (b) Magnified view of region b in (a), showing interface structure. (c) Further magnified image of (b), highlighting reaction layer and interfacial features. (d) Magnified view of region d in (a). (e) Further magnified image of (d), focusing on pore distribution and interfacial microstructural characteristics.

layer was slightly thicker, and the precipitated phases were more pronounced. The formation of the reaction layer effectively sealed the surface pores, mitigating the risk of localized infiltration. Furthermore, the original porous structure beneath this continuous and dense reaction product layer was preserved, ensuring that the thermal insulation properties of the coating remained uncompromised. This indicates that although the rough coating surface provided more potential pathways for infiltration, the YYbGdZO coating formed a robust physical barrier via a rapid interfacial reaction, effectively preventing further ingress of the melt.

Figure 6 presents the cross-sectional microstructure of the surface-polished YYbGdZO coating under the same corrosion conditions. In contrast to the rough surface, the CMAS-E/coating interface on the smooth surface appears exceptionally flat and regular (Fig. 6(a)). Furthermore, the reaction product layer formed on the smooth surface is considerably denser and more continuous, exhibiting greater uniformity and forming a thin yet highly effective barrier layer. This phenomenon reveals the excellent intrinsic reactivity of the YYbGdZO coating: Even on the smooth surface where the melt spreads more rapidly, the interfacial reaction is still capable of quickly forming a complete passivation layer, thereby inhibiting melt infiltration and corrosion of the coating material. Regardless of the location—whether at the edge or in the center of the melt/coating contact interface—when a small amount of CMAS-E melt infiltrated the vertical pores on the coating surface, it reacted *in situ* with the YYbGdZO material on the pore walls, and the resulting reaction products filled the entire pore (Figs. 6(c) and 6(e)). This "reaction self-filling" phenomenon provides compelling evidence that the reaction-crystallization rate of the YYbGdZO coating surpasses the infiltration rate of the melt. Even when the melt has already penetrated microdefects, the coating is able to "self-heal" them through rapid chemical reactions, thereby completely severing the infiltration pathways.

A comprehensive comparison of the microstructural responses of the two coating types led to the conclusion that while surface roughness significantly influences the macroscopic behavior of melt spreading and interfacial reactions, it does not alter the core anti-infiltration mechanism of the YYbGdZO coating. On the rough surface, the coating seals the porous structure by forming a reaction-crystallization layer; on the smooth surface, where the melt spreads more readily, the coating forms a thin, uniform reaction layer and rapidly fills preexisting defects, demonstrating highly effective resistance to environmental deposit corrosion. This confirms that the protective mechanism of the YYbGdZO coating relies primarily on its rapid reaction kinetics.

In conclusion, while surface roughness significantly influences the macroscopic expression of melt spreading and interfacial reactions, it does not alter the core anti-infiltration mechanism of the YYbGdZO coating, which is rooted in its intrinsic high chemical reactivity. On a rough surface, the physical topography and chemical reactions act synergistically: Its complex peak-valley structure physically hinders melt spreading, whereas the reaction preferentially nucleates in pores and depressions to progressively build a conformal barrier. In contrast, on a smooth surface, protection relies almost entirely on extremely fast chemical reaction kinetics, where the rate of reaction-crystallization must outpace the more rapid melt spreading rate, resulting in a flatter, more uniform reaction layer. Therefore, although the macroscopic processes differ, both scenarios ultimately validate that the coating's success depends on its rapid reaction capability. More importantly, the performance of the smooth surface provides the most compelling evidence that the intrinsic chemical reactivity of a material is the fundamental guarantee of its exceptional corrosion resistance.

3.3 Interface failure of double-layered TBCs under CMAS-E corrosion infiltration

3.3.1 Phase and morphology evolution of the MRE-SZ/CMAS-E composite system

To fully appreciate the superiority of the proposed dynamic defense mechanism, first establishing a relevant comparative baseline is instructive. MRE-SZ coatings exhibit significant application potential in high-temperature environments because of their low thermal conductivity and enhanced phase stability. To optimize their overall durability, they are often combined with a YSZ layer to form double-layer ceramic TBCs [32]. However, its behavior under the particularly harsh low-Ca/Si-ratio CMAS-E environment has not yet been fully clarified. Therefore, this section aims to systematically investigate the response pathway of an MRE-SZ/YSZ double-layer coating when exposed to a CMAS-E melt. As the first step in this investigation, this subsection employs a powder-compact reaction method, which is designed to

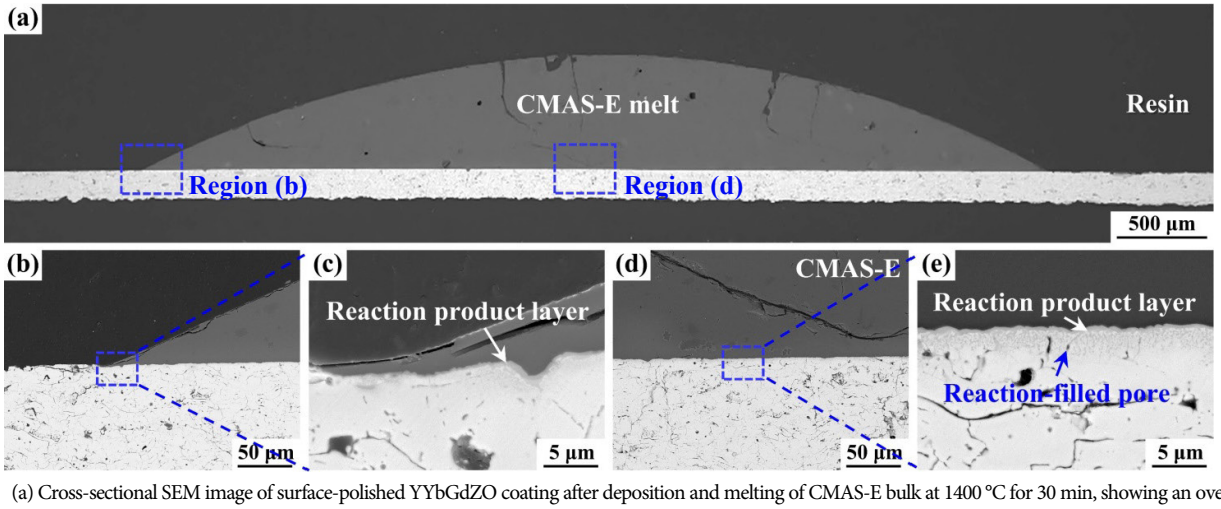

Fig. 6 (a) Cross-sectional SEM image of surface-polished YYbGdZO coating after deposition and melting of CMAS-E bulk at 1400 °C for 30 min, showing an overview of coating/melt interface. (b) Magnified view of region b in (a). (c) Further magnified view of (b), highlighting continuous reaction layer and interface characteristics. (d) Magnified view of region d in (a). (e) Further magnified view of (d), focusing on pore distribution and interfacial microstructural features.

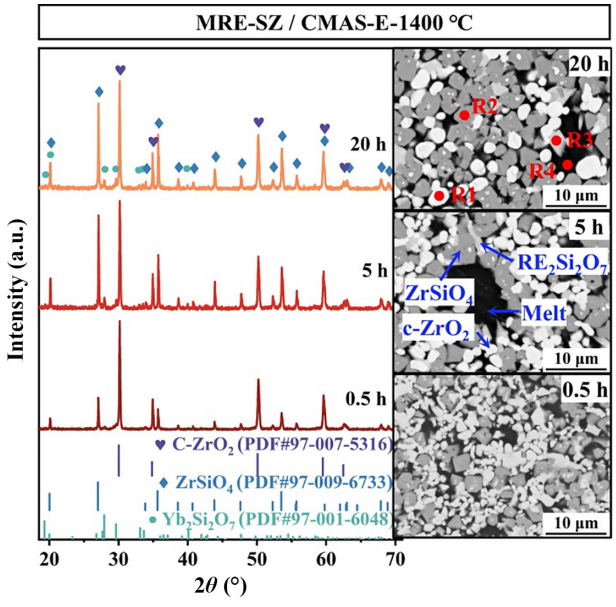

Fig. 7 XRD patterns and microstructure evolution: XRD and SEM images of MRE-SZ coating after interaction with CMAS-E at 1400 °C for different time intervals (0.5, 5, and 20 h).

isolate the fundamental chemical interactions from complex microstructural effects, to first identify the intrinsic reaction products and their evolutionary pathways.

Figure 7 displays the XRD patterns and SEM images of the MRE-SZ/CMAS-E powder mixture after reacting at 1400 °C for different durations (0.5, 5, and 20 h). The XRD patterns reveal that the primary reaction products between the MRE-SZ material and the CMAS-E melt are $ZrSiO_4$ and cubic zirconia (c-ZrO_2). As the reaction time increased from 0.5 to 5 h, the intensity of the $ZrSiO_4$ diffraction peaks increased significantly, indicating a substantial increase in the volume fraction of the $ZrSiO_4$ phase. When the reaction time is further extended to 20 h, the peak intensities show no significant change, suggesting that the interfacial reaction has approached completion.

In the SEM images, the morphological evolution of the corrosion products is clearly visible, providing direct evidence of a vigorous chemical reaction between MRE-SZ and the CMAS-E melt. Combined with EDS analysis (Table 5), the white spherical phase is identified as c-ZrO_2, the gray angular phase as $ZrSiO_4$, and the black regions as residual melt, whereas localized light-gray phases are identified as RE silicates. The distinct interfaces between the various phase particles and the melt are characteristic of a typical dissolution–reprecipitation mechanism: Constituents from the MRE-SZ coating (such as Zr^{4+} and RE^{3+}) first dissolve into the CMAS-E melt. When the local concentration reaches supersaturation, more thermodynamically stable new phases ($ZrSiO_4$, c-ZrO_2, and $RE_2Si_2O_7$) precipitate at the solid–liquid interface.

In summary, the interaction between MRE-SZ and CMAS-E at 1400 °C is a time dependent, dynamic reaction process governed by a dissolution–reprecipitation mechanism. Analysis of the phase composition and its evolution over time demonstrated that the reaction process transformed the low-melting-point CMAS-E melt into stable ceramic phases composed of high-melting-point RE silicates and zircon. The evolution of the reaction products of the coating provides theoretical support, on the basis of phase evolution, for its corrosion resistance.

3.3.2 Microstructural evolution of MRE-SZ/YSZ double-layered TBCs under CMAS-E corrosion infiltration

Having identified the primary reaction products between MRE-SZ and CMAS-E in the preceding subsection, a critical question arises: How do these intrinsic chemical reactions manifest within an actual coating, which possesses a complex porous and lamellar architecture? This subsection therefore aims to elucidate how the inherent microstructure of a coating interacts with these chemical reactions to ultimately govern its microstructural degradation and failure pathway.

Figure 8 shows the microstructural evolution and elemental distribution of the MRE-SZ/YSZ double-layer coating after reacting with the CMAS-E melt for various durations (0.5, 5, 20, and 50 h). The microstructure and elemental distribution of the coating changed significantly as the reaction time increased. At 0.5 h (Fig. 8(a)), the coating surface primarily showed incipient signs of melt infiltration (Fig. 8(a2)). The melt penetrated the MRE-SZ layer via capillary action, filled pores, and cracks, and generated a small amount of gray corrosion products in localized areas on the top surface. However, no obvious structural changes were observed, indicating that although the melt had begun to infiltrate, the overall structure of the coating remained largely intact in the short term. Notably, although a small amount of precipitated phase can be observed filling individual pores in this initial stage (Fig. 8(a1)), this sealing effect is localized and discontinuous. These isolated precipitates fail to rapidly coalesce into a complete and dense infiltration barrier. Consequently, the CMAS-E melt can easily bypass these locally blocked areas and continue to penetrate deep into the interior of the coating through the abundant interconnected pore network. This ineffective early-stage sealing is one of the key reasons why the MRE-SZ coating fails to effectively resist CMAS-E corrosion and stands in stark contrast to the continuous barrier formed by the YYbGdZO coating, as discussed in Sections 3.3.3 and 3.5.2. After 5 h of reaction (Fig. 8(c)), the penetration depth of the CMAS-E melt continued to increase (Fig. 8(c2)), triggering a significant interfacial reaction in the top region of the MRE-SZ layer. High-magnification images (Figs. 8(c1) and 8(c2)) show that the melt infiltrated along pore channels and preferentially dissolved grain boundaries, accompanied by the loss of RE elements from within the grains. In the context of the dissolution–reprecipitation mechanism, this phenomenon indicates that components from the melt (e.g., SiO_2) reacted with elements in the MRE-SZ coating, leading to continuous dissolution of the grain boundaries and accelerating the migration and dissolution of elements from the

Table 5 Elemental compositions (at%) of points indicated in Fig. 7

Sample	Point	Composition (at%)												Phase
		Si	Ca	Na	Al	Mg	K	Fe	Y	Yb	Gd	Zr	O	
MRE-SZ/CMAS-E	R1	—	—	—	—	—	—	—	3.6	1.1	0.9	24.2	70.3	Fluorite
	R2	14.1	—	—	—	—	—	—	—	—	—	14.1	71.8	Zircon
	R3	17.1	—	—	—	—	—	—	9.5	2.9	2.6	—	67.9	Silicate
	R4	20.5	1.2	2.6	5.8	0.5	1.7	0.5	—	—	—	—	67.2	Melt

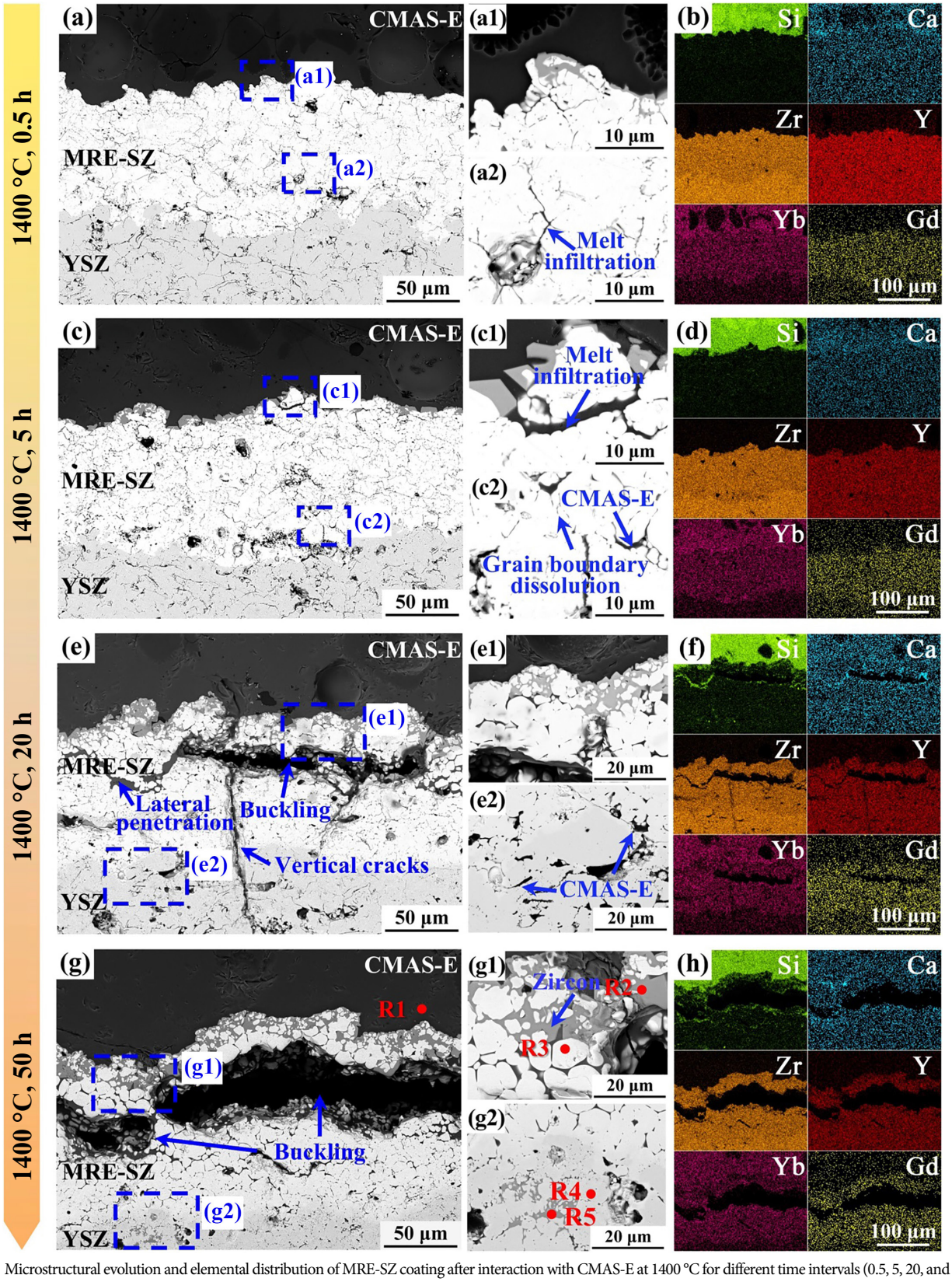

Fig. 8 Microstructural evolution and elemental distribution of MRE-SZ coating after interaction with CMAS-E at 1400 °C for different time intervals (0.5, 5, 20, and 50 h).

grain interiors. Over time, this dissolution-reprecipitation reaction could further exacerbate coating corrosion and degrade structural integrity. When the corrosion time reached 20 h (Fig. 8(e)), the damage mode began to transition from chemical corrosion to thermomechanical coupled failure. The top layer of the double-layer coating exhibited significant local deformation, including the formation of lateral melt penetration channels that traversed the lamellar splats and buckled. The extensive melt penetration and continuous reaction led to stress accumulation, which induced significant deformation and cracking of the coating. Concurrently, the stress concentration promoted the formation of vertical cracks that traversed the reaction layer. These newly formed cracks

provided pathways for further melt infiltration, accelerating corrosion evolution. The Si elemental maps in Fig. 8(f) shows that the melt penetrated through the MRE-SZ layer and advanced into the YSZ layer, further demonstrating the inadequate penetration resistance of the MRE-SZ layer against CMAS-E. The thermal expansion mismatch was a key driving force for the deformation and failure of the coating. After 50 h of reaction (Fig. 8(g)), the melt continued to dissolve the coating grains, leading to more pronounced buckling within the infiltrated region. EDS analysis (Table 6) revealed that in the top region of the coating, SiO_2 from the melt reacted with zirconium from the MRE-SZ layer to form a zircon phase, which precipitated along the infiltration channels. However, owing to the slow crystallization rate of zircon, it fails to form a uniform, continuous protective layer in a short time, allowing the melt to continue infiltration. As shown in Fig. 8(g2) and the elemental maps, the melt penetrated deep into the bottom of the coating, and a discontinuous zircon phase formed both at the top of the MRE-SZ layer and within the YSZ layer. Notably, no apatite phase was observed among the reaction products, which contrasts with the common formation of apatite in standard CMAS reactions reported in the literature [36,37]. This is likely due to the lower Ca/Si ratio of CMAS-E, which leads to the formation of different corrosion products and further affects the corrosion resistance of the coating. Furthermore, the precipitation of the zircon phase was primarily concentrated in the surface region of the MRE-SZ layer, with limited precipitation deeper within the coating. This can be attributed to the local reaction saturation state. Specifically, owing to the limited amount of melt that can infiltrate the interior of the coating, components from the melt, such as Y_2O_3, reach local saturation equilibrium more quickly, inhibiting further dissolution–corrosion reactions and allowing the composition of the internal regions to remain relatively stable [11]. Additionally, as the melt reacted with the coating at the surface, it preferentially consumed SiO_2 to form zircon, leading to a decrease in the Si content of the melt that penetrated deeper. This reduced the opportunity for further reactions between Zr and SiO_2. The combination of these factors not only slowed the melt infiltration rate but also caused the corrosion products to precipitate mainly near the MRE-SZ surface. Moreover, the deeper regions of the coating, where melt infiltration was limited and the reaction kinetics were slower, experienced only minor compositional changes. This created the conditions for stress concentration that precipitated the subsequent buckling failure.

In summary, the MRE-SZ/YSZ double-layer coating exhibited poor resistance to CMAS-E corrosion. As the reaction time increased, the melt penetration depth progressively increased, and grain boundary corrosion intensified, ultimately leading to large-scale infiltration and buckling failure of the coating. This process reveals the inadequacy of the MRE-SZ coating in resisting CMAS-E corrosion and provides a valuable reference for the design of new YYbGdZO materials and biomimetic multilayer coatings.

3.3.3 CMAS-E corrosion-induced buckling and delamination of double-layered TBCs

The failure process initiated by CMAS-E corrosion begins with the contact and infiltration of the melt with the MRE-SZ coating surface at high temperatures. Figure 9 illustrates the evolution of this failure. In the initial stage, the molten CMAS-E, driven by capillary forces, infiltrates the inherent intersplat pores and crack networks of the plasma-sprayed coating. It engages in direct thermochemical interactions with the MRE-SZ ceramic layer (ZrO_2–$10Y_2O_3$–$5Yb_2O_3$–$5Gd_2O_3$) at the interface, a process characterized by elemental dissolution and interdiffusion, accompanied by the nucleation of a small amount of zircon phase. In the subsequent stage, as melt infiltration and coating dissolution continue, zircon crystals precipitate and grow in the surface region. The experimental results show that the reaction between the coating and the CMAS-E melt predominantly results in the formation of zircon ($ZrSiO_4$), with almost no formation of RE silicates or apatite. This corrosion product is closely linked to the compositional characteristics of the CMAS-E melt (low Ca/Si

Table 6 Elemental compositions (at%) of points indicated in Fig. 8

Sample	Point	Composition (at%)												Phase
		Si	Ca	Na	Al	Mg	K	Ti	Fe	Y	Yb	Gd	Zr	O	
MRE-SZ + YSZ	R1	30.1	0.7	1.3	3.5	0.3	0.9	0.0	0.3	—	—	—	—	63.0	Melt
	R2	17.9	—	—	—	—	—	—	—	—	—	—	21.1	61.0	Zircon
	R3	—	—	—	—	—	—	—	—	5.1	1.7	1.3	30.6	61.3	Fluorite
	R4	—	—	—	—	—	—	—	—	2.6	—	—	34.8	62.6	YSZ
	R5	16.2	—	—	—	—	—	—	—	—	—	—	19.2	64.7	Zircon

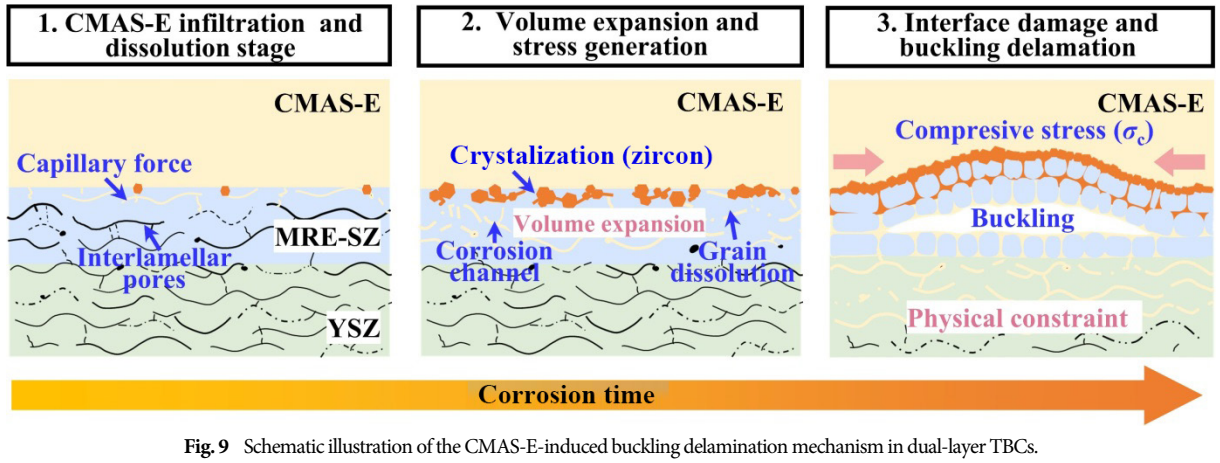

Fig. 9 Schematic illustration of the CMAS-E-induced buckling delamination mechanism in dual-layer TBCs.

ratio) and the specific composition of the MRE-SZ coating, which collectively dictate the final product phase. First, from a thermodynamic perspective, the formation of the apatite phase (the general formula $Ca_2RE_8(SiO_4)_6O_2$) is significantly affected by the Ca^{2+} concentration in the melt. The formation and stability of apatite require an ample supply of calcium ions from the melt [30]. However, the CMAS-E melt used in this study has a low Ca/Si ratio (low basicity), meaning that the chemical potential of Ca^{2+} is insufficient to drive and stabilize the apatite crystal structure. This is particularly true for RE cations with smaller ionic radii, for which the thermodynamic driving force to form apatite in a low-calcium melt is even weaker [38]. Furthermore, the different ionic radii of RE ions also lead to varying tendencies for product formation. It has been reported that in systems containing Yb, Y, and Gd ions, the stability of corrosion products differs: the Ca-RE apatite phase rarely forms in systems with smaller Yb^{3+} ions, whereas it forms more readily in systems with larger Gd^{3+} ions; for Y^{3+}, which is an intermediate, the coexistence of RE silicates and apatite may occur [39]. Second, from a kinetic standpoint, the preferential precipitation of the zircon phase stems from the different dissolution and diffusion rates of various cations in the melt. When molten CMAS-E contacts the MRE-SZ coating, its constituents, including Zr^{4+} and various RE cations (RE^{3+}), begin to dissolve into the melt. Studies have shown that the solubility of Zr^{4+} in silicate melts is much lower than that of RE^{3+} ions such as Y^{3+} [40,41]. This means that the melt can rapidly reach local supersaturation with Zr^{4+} at the dissolution front of the MRE-SZ grains, providing a strong kinetic driving force for the nucleation and growth of the zircon phase. In contrast, although RE ions also dissolve, their higher solubility prevents their concentrations from reaching saturation, thus precluding the formation of phases such as RE silicates or apatite. For MRE-SZ, the total RE content is lower than that in previously reported highly doped zirconia systems [42], and the codoping of Y, Yb, and Gd may dilute the concentration of any single RE element, making it difficult to reach the threshold required for apatite nucleation. In this process, Zr^{4+} rapidly accumulates and reacts with SiO_2, preferentially forming zircon ($ZrSiO_4$). This reaction consumes SiO_2 near the interface, preventing the formation of other potential products and establishing zircon as the primary product. This result indicates that the different dissolution/diffusion and saturation behaviors of the RE ions and Zr in the melt led to the preferential and stable precipitation of the zircon phase.

As the reaction proceeds, Zr and Si are continuously consumed from the melt and precipitate as zircon. The deposition of these zircon crystals within the pores of the coating caused channels, which were originally filled with melt, to be gradually occupied by expanding crystals. Constrained by the surrounding ceramic skeleton, the volume expansion induced by this localized crystallization cannot be freely accommodated, thereby generating additional expansion pressure and accumulating local stress. The precipitation of zircon inhibits further CMAS-E infiltration by blocking pores and introduces additional stress into the coating because of the volume effect. When the accumulated local compressive stress (σ_c) exceeds the critical strength of the coating, the system enters the failure stage: the zircon-rich crystallized surface layer delaminates at its interface with the less affected zone below, forming a subsurface crack. This drives the buckling of the upper zircon-containing thin layer, which ultimately bulges and propagates from within the coating. The literature reports that under similar CMAS infiltration conditions, the melt-infiltrated surface region generates significant compressive stress upon cooling due to thermal expansion mismatch, which can induce interfacial cracking within the coating [43–45]. The CMAS corrosion process fundamentally alters the mechanical properties of the TBC surface, creating a classic heterogeneous layered structure. The reaction and melt-filling transform the initially porous, strain-tolerant structure into a dense, highly stiff, and highly brittle composite layer. When the in-plane compressive stress in this rigid layer accumulates to a critical value, it deforms into periodic, wave-like wrinkles to release strain energy. This process, known as elastic buckling, is an energy release mechanism that converts compressive strain energy into bending strain energy. The onset of buckling marks the transition of the coating from a two-dimensional (2D) compressed state to a 3D unstable state and directly leads to subsequent delamination. During buckling, significant interfacial tensile and shear stresses are generated at the crests and troughs of the waves. These stress concentration effects strongly promote the initiation and propagation of interfacial cracks, ultimately leading to the catastrophic spallation of the corroded layer.

In summary, the zircon crystals formed during CMAS-E corrosion and their associated volume expansion induce significant compressive stress accumulation within the coating. When this stress concentration exceeds the interfacial bonding strength, it leads to buckling deformation, subsurface crack propagation, and eventual spall failure. This evolutionary process reveals that the synergy between chemical corrosion and mechanical mismatch is the fundamental failure mechanism of the double-layer TBC in a high-temperature CMAS-E environment.

3.4 Microstructure and mechanical properties of bioinspired multilayer coatings

The failure process of the MRE-SZ/YSZ double-layer coating revealed in the preceding section indicates that its degradation originates from the limited chemical reactivity and poor infiltration resistance of the MRE-SZ top layer, which ultimately leads to catastrophic buckling and delamination. This finding suggests that although double-layer TBCs—comprising a novel top coat combined with a YSZ base layer—can alleviate thermal mismatch and enhance overall performance [32], they remain prone to failure when exposed to complex CMAS-E environments with low Ca/Si ratios. Conventional "passive defense" or single "sacrificial reaction" strategies are insufficient to ensure both chemical stability and mechanical reliability simultaneously. Building upon this understanding, the present study draws inspiration from natural biomineralization processes to develop a novel "active, dynamic, and multifaceted" biomimetic defense strategy designed to realize adaptive resistance to high-temperature corrosive environments via functional complementarity between layers and dynamic control of interfacial reactions.

The nacreous layer structure and its barrier mechanism inspired the design of this work. As illustrated in Fig. 10, when a foreign object enters the shell of a mollusk, it stimulates the secretion of nacre, which encapsulates the object layer by layer to form a defensive barrier known as a pearl [46–48]. This process is, in essence, a highly efficient, self-adaptive defense mechanism: upon perceiving an external threat, the system actively responds by constructing a robust isolation barrier *in situ*. This study aims to translate this biological principle into a functional design for protective coatings, whereby upon encountering a CMAS-E melt, the coating spontaneously reacts to form a dense barrier that provides both physical blockade and chemical passivation, thereby actively inhibiting corrosion. On the basis of this biomimetic concept, we designed a multifunctional coating system composed

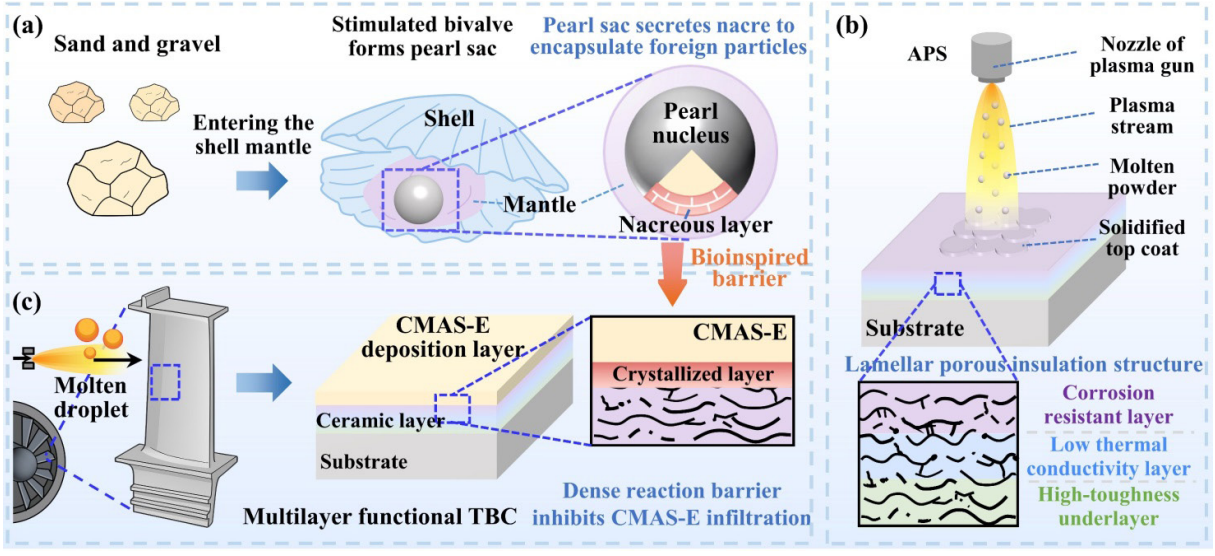

Fig. 10 Schematic illustration of design concept, fabrication process, and dynamic defense mechanism of the bioinspired multilayer TBC: (a) Design is inspired by biomineralization process of nacre encapsulating foreign particles to form a pearl. (b) Fabrication of functionally zoned multilayer ceramic coating structure via APS. (c) In-service dynamic defense mechanism where top layer of bioinspired TBC actively reacts with molten CMAS-E to form a dense, crystalline, infiltration-resistant layer *in situ*, effectively suppressing melt penetration.

of three ceramic layers. Through functional partitioning, the chemical reactivity required for CMAS-E resistance is decoupled from the mechanical toughness needed for long-term service, and both are integrated into a single system [49]. As shown in Fig. 10(b), this multilayer structure is fabricated via the APS technique; its lamellar, porous structure is advantageous for reducing the thermal conductivity and enhancing the strain tolerance. The functional roles of each layer are as follows: the top layer serves as the core functional layer that directly interacts with the CMAS-E melt. A MRE (Gd–Yb–Y) costabilized zirconia (YYbGdZO) material was employed on the basis of previous research [31]. The multicomponent codoping design is intended to impart the ability to react rapidly and adaptively with CMAS-E. Its core function is to be "triggered" by the molten CMAS-E at 1400 °C, forming a unique, dense, dual-phase composite barrier layer *in situ* via a solid-liquid reaction, as depicted in Fig. 10(c). The selection of MRE-SZ, a material with low thermal conductivity, as the intermediate transition layer is a key aspect of our "functionally graded" design concept. The core function of MRE-SZ is to provide a smooth transition in chemical and mechanical properties between the top YYbGdZO and bottom YSZ layers. Its intermediate chemical composition helps to enhance interlayer compatibility, whereas the graded mechanical properties are beneficial for mitigating stress concentrations at the interfaces. Additionally, the intrinsically low thermal conductivity of MRE-SZ also contributes to the overall thermal insulation performance. Therefore, the MRE-SZ layer functions as more than just a simple insulating layer. It is a sophisticated "graded buffer zone" designed to enhance the structural stability and durability of the entire coating system by smoothing these property transitions. The bottom tough layer is composed of conventional YSZ, which possesses high fracture toughness [50,51]. In this design, the function of YSZ is not to directly resist chemical corrosion but to serve as a robust mechanical support for the entire coating system. This material provides excellent strain tolerance and resistance to thermal cycling spall, ensuring the overall reliability of the coating under harsh operating conditions.

To realize the "pearl-like" dynamic defense design concept, a functionally partitioned YYbGdZO/MRE-SZ/YSZ three-layer ceramic coating was successfully fabricated via the APS technique. Figure 11 presents a comprehensive characterization of the microstructure, phase composition, elemental distribution, and mechanical properties of the as-prepared coating. The fractured cross-sectional morphology of the coating, shown in Fig. 11(a), reveals that columnar grains grow perpendicular to the substrate, with vertical cracks running through them. This microstructure is beneficial for releasing stresses generated by thermal expansion mismatch during thermal cycling, thereby enhancing the thermal shock resistance and durability of the coating. The polished cross-sectional morphology, depicted in Fig. 11(b), clearly shows the layered structure comprising the top YYbGdZO, intermediate MRE-SZ, and bottom YSZ layers, with distinct and well-bonded interfaces. Within each layer, a typical lamellar stacked morphology characteristic of APS deposition is observed, which is characterized by a network of intersplat pores and microcracks, resulting in an average porosity of approximately 9.45%±1.9%, as determined by image analysis. This porous, lamellar structure not only endows the coating with excellent thermal insulation properties but also enhances its overall fracture toughness through crack energy dissipation mechanisms. Figure 11(c) shows the elemental maps of the cross section, which confirm the designed elemental gradient distribution, indicating that the APS process successfully constructed the intended chemically and functionally graded architecture.

The phase composition of each layer was analyzed via XRD, and the results are shown in Fig. 11(d). All three layers—YYbGdZO, MRE-SZ, and YSZ—exhibit a single-phase structure. The metastable tetragonal phase (t′) formed in the APS-prepared YSZ coating possesses excellent phase stability, which prevents the destructive volume expansion associated with the t′ → m phase transformation during thermal cycling. The XRD pattern of the MRE-SZ intermediate layer matches well with that of c-ZrO_2, indicating that the introduction of multiple RE elements successfully retained the high-temperature stable cubic phase down to room temperature. Compared with those of the YSZ layer, its diffraction peaks slightly shift to lower angles, which is attributed to the substitution of Zr^{4+} ions by various RE ions in the ZrO_2 lattice, causing an increase in the lattice parameter. The diffraction peaks of the top YYbGdZO layer also present a typical

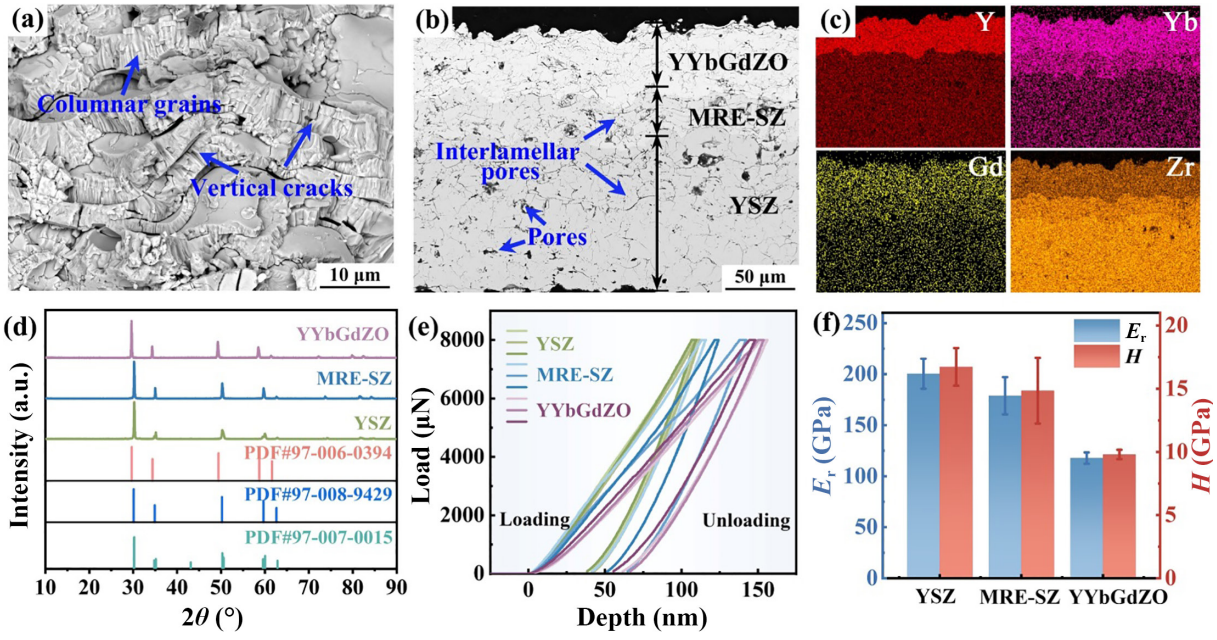

Fig. 11 Microstructure, phase composition, elemental distribution and mechanical properties of bioinspired multilayer TBCs: (a) fracture morphology showing columnar grains and vertical cracks; (b) cross-sectional morphology with interlamellar pores; (c) elemental mapping of Y, Yb, Gd, and Zr; (d) XRD patterns; (e) nanoindentation load–displacement curves; (f) comparison of nanoindentation-derived H and E_r.

cubic fluorite structure. The shift of the YYbGdZO peaks to lower angles is the most significant among the three layers. According to Bragg's law ($n\lambda = 2d\sin\theta$, where λ is the X-ray wavelength, d is the interplanar spacing, and θ is the Bragg diffraction angle), a decrease in the diffraction angle corresponds to an increase in the d-spacing, providing strong evidence of more pronounced lattice expansion due to the codoping of multiple large-radius RE ions (Gd^{3+}, Y^{3+}, and Yb^{3+}). In summary, the XRD results confirm the successful fabrication of a multilayer coating system composed of three distinct, yet single-phase and highly stable, ceramic compositions. This structural design, which is free from the risk of detrimental phase transformations, along with the systematic change in lattice parameters induced by the elemental gradient, provides a solid phase foundation for the long-term service and functional performance of the coating in extremely high-temperature environments.

Figure 11(e) further presents the nanoindentation load–displacement curves for each layer, which exhibit distinctly different indentation responses. Under the same load, the top YYbGdZO layer shows the largest indentation displacement, whereas the bottom YSZ layer is the smallest, with the intermediate MRE-SZ layer falling in between. This indicates that the hardness and stiffness are the lowest in the top layer and gradually increase from the surface to the interior. A comparison of the hardness (H) and reduced elastic modulus (E_r) obtained from the nanomechanical tests is shown in Fig. 11(f). The bottom YSZ layer has the highest average H (16.7±1.5 GPa) and E_r (200±14.7 GPa), followed by the intermediate layer, whereas the top layer has the lowest H (9.8±0.4 GPa) and E_r (117.8±5.5 GPa). Specifically, the H and E_r of the YSZ layer are both 1.7 times greater than those of the top layer. This through-thickness gradient in mechanical properties is one of the core mechanical features of this biomimetic design. The graded property match between layers prevents stress concentration at the interfaces, highlighting the advantage of synergistic work among the functional layers. In conclusion, the structural design of the biomimetic multilayer TBC not only possesses the structural features required for conventional TBCs—such as low thermal conductivity and high strain tolerance—and excellent high-temperature phase stability but also establishes a graded structure with a smooth transition in mechanical properties through its sophisticated functional partitioning. This optimized structure lays a solid foundation for achieving an effective and durable dynamic defense against CMAS-E corrosion.

3.5 Corrosion behavior of bioinspired multilayer coatings induced by CMAS-E

3.5.1 Phase and morphology evolution in the YYbGdZO/CMAS-E composite system

Following the clarification of the design concept and functional gradient architecture of the biomimetic multilayer coating in the previous section, its effectiveness under CMAS-E corrosion conditions must be validated. Accordingly, this section first identifies the intrinsic reaction products between the core functional material YYbGdZO and the CMAS-E melt through a powder mixture reaction approach, thereby decoupling the fundamental chemical interactions from the complex microstructural effects present in actual coatings (such as porosity and layered morphology). A detailed analysis of the phase evolution and microstructural transformations of the biomimetic coating under CMAS-E attack was subsequently conducted to elucidate its distinctive dynamic defense mechanism and how it successfully avoids the failure modes observed in the MRE-SZ system.

Figure 12 shows the results of the phase composition and microstructural evolution of the YYbGdZO/CMAS-E powder mixture after reacting at 1400 °C for different durations (0.5, 5, and 20 h). The XRD patterns reveal that the primary reaction products between the YYbGdZO material and the CMAS-E melt are $RE_2Si_2O_7$ and c-ZrO_2. As the reaction time increased, the intensities of the characteristic diffraction peaks remained largely stable, and no new crystalline phases emerged, indicating that the

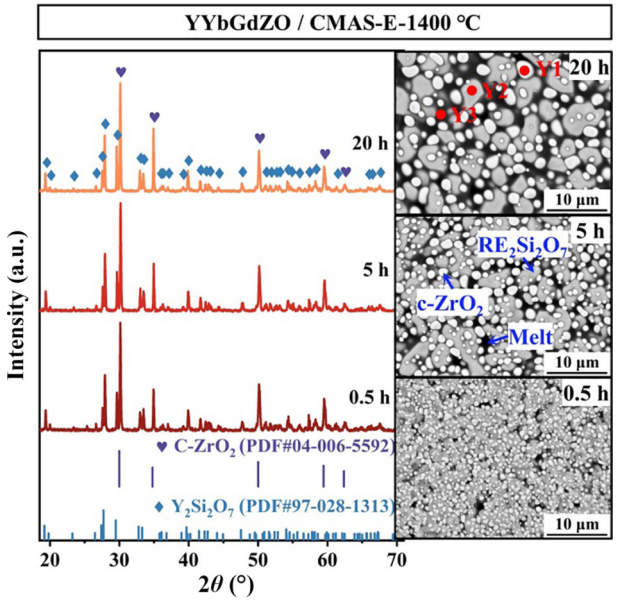

Fig. 12 XRD patterns and microstructure evolution: XRD and SEM images of YYbGdZO coating after interaction with CMAS-E at 1400 °C for different time intervals (0.5, 5, and 20 h).

system completed its main phase transformations within a short period and that the interfacial reaction approached equilibrium. The SEM images further reveal the morphological evolution of the corrosion products, providing direct evidence of the vigorous reaction between YYbGdZO and the CMAS-E melt. Combined with EDS compositional analysis (Table 7), the white spherical phase, which is rich in Zr, Y, Yb, and Gd but contains almost no Si, is identified as either reprecipitated or incompletely dissolved, compositionally stable c-ZrO_2 (fluorite). The gray phase, which contains high concentrations of Si and RE elements, is confirmed as the $(Y,Yb,Gd)_2Si_2O_7$ phase. The black regions, which retain the primary elements of CMAS-E (Si, Al, Ca, Na, Mg, and K), correspond to the residual glassy melt after the reaction. The distinct interfaces between the various phase particles and the melt indicate that the reaction process primarily follows a "dissolution–reprecipitation" mechanism. In this process, the coating is first wetted and partially dissolved by the melt at high temperature, releasing RE and zirconium ions into the melt. When local supersaturation is reached, the thermodynamically stable RE silicate and c-ZrO_2 phases precipitate and grow at the interface. As the reaction time increased, the morphology of these phases coarsened, but their phase types remained unchanged.

In summary, the interaction between the YYbGdZO coating and CMAS-E at 1400 °C is governed primarily by a dissolution–reprecipitation mechanism, and the resulting c-ZrO_2 and $RE_2Si_2O_7$ reaction products possess high thermodynamic stability. This result indicates that the coating can maintain a stable phase structure even under prolonged high-temperature corrosion, which positively contributes to its enhanced resistance against CMAS corrosion.

3.5.2 Microstructural evolution of bioinspired multilayer coatings induced by CMAS-E

To further elucidate the formation and evolution of the biomimetic dynamic defense barrier, the cross-sectional microstructures of the multilayer coating after CMAS-E corrosion at 1400 °C for various durations were characterized, and the results are presented in Fig. 13. As the corrosion time increased from 0.5 to 100 h, the reaction layer progressively thickened, and its internal microstructure underwent significant evolution. In the initial stage of corrosion (0.5 h), the process was characterized primarily by melt infiltration and rapid interfacial crystallization. A reaction layer with a thickness of approximately 3.5±0.5 μm formed on the coating surface (Figs. 13(a) and 13(a1)). A vigorous reaction occurred immediately upon contact between the CMAS-E melt and the coating, forming an extremely thin and continuous layer of precipitated phases at the solid–liquid interface, whereas the region beneath consisted of a diffusion-affected zone formed by dissolution–reprecipitation. Concurrently, a few plugged pores and intersplat pores were observed within the reaction layer, indicating that rapid crystallization upon contact with the melt sealed the surface pores and inhibited further melt infiltration. When the corrosion time was extended to 5 h (Figs. 13(c) and 13(c1)), the reaction layer continued to thicken, and two types of precipitated phases with different contrasts formed in the top region. The precipitates near the melt side exhibited a continuous and dense distribution, whereas those closer to the coating tended to grow preferentially in pores or depressions. High-magnification SEM and EDS results (Fig. 13(d)) indicate that these precipitated phases effectively blocked melt infiltration and elemental diffusion, demonstrating the high reactivity of the YYbGdZO coating and the barrier effect of the continuous precipitated phases. Moreover, the original porous structure was preserved to a certain extent, which helped maintain the thermal insulation properties and strain tolerance of the coating. By 20 h (Figs. 13(e) and 13(e1)), the reaction layer had thickened to 10.8±0.9 μm, and the continuous, dense barrier at the interface exhibited a more distinct double-layer morphology. EDS point analysis (G1–G4), as listed in Table 8, indicated that the reaction layer was composed of multiple RE silicate, a Ca-rich apatite phase, and a Zr-rich fluorite-structured phase. The formation of this multiphase composite structure originated from the synergistic effect of melt infiltration and the outward diffusion of RE elements. After further extending the corrosion time to 50 h (Figs. 13(g) and 13(g1)), the reaction layer reached a thickness of 15.4±0.9 μm, and the RE silicate layer, the apatite layer, and the transitional zone composed of apatite/fluorite progressively thickened. Elemental maps revealed that this reaction layer effectively blocked the infiltration of active components such as Ca and Si from the melt.

When the corrosion time was extended to 100 h (Figs. 13(i) and 13(i1)), the reaction layer further thickened to 18.8±1.5 μm, and the multilayered reaction barrier—composed of an outer RE silicate layer, an inner apatite layer, and an apatite/fluorite composite transition zone—became mature and stable. This barrier significantly reduced the dissolution rate of the ZrO_2 matrix and prevented infiltration and corrosion of the CMAS-E melt.

Table 7 Elemental compositions (at%) of points indicated in Fig. 12

Sample	Point	Composition (at%)											Phase
		Si	Ca	Na	Al	Mg	K	Y	Yb	Gd	Zr	O	
YYbGdZO/ CMAS-E	Y1	—	—	—	—	—	—	5.6	1.5	1.1	21.1	70.8	Fluorite
	Y2	17.7	—	—	—	—	—	11.8	2.3	2.5	—	65.7	RE silicate
	Y3	19.3	0.7	1.8	6.0	0.3	1.9	2.5	—	—	—	67.6	Melt

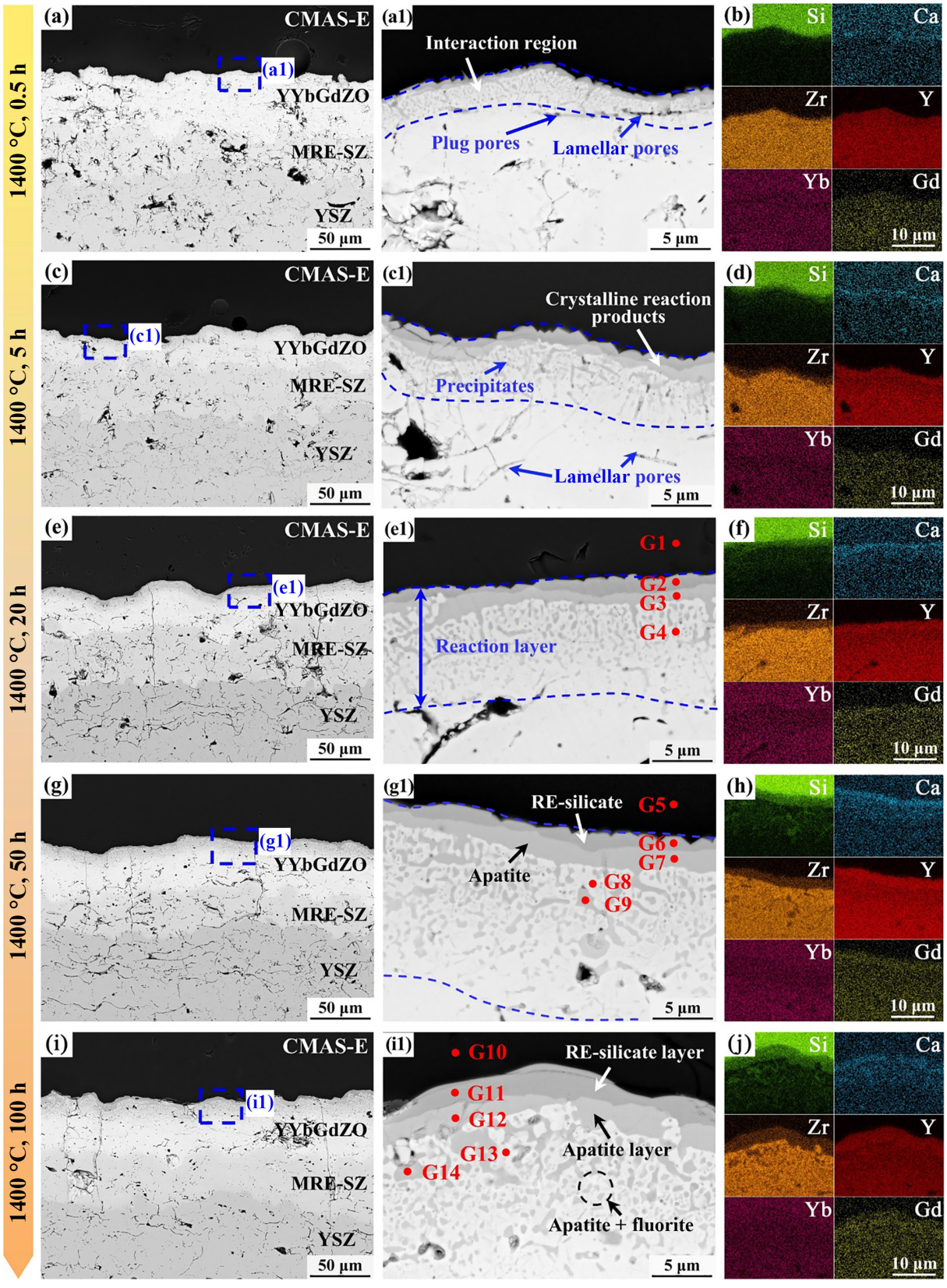

Fig. 13 Cross-sectional SEM micrographs and corresponding EDS elemental maps showing microstructural evolution of the bioinspired multilayer TBC after corrosion by CMAS-E at 1400 °C for different durations (0.5, 5, 20, 50, and 100 h): (a, c, e, g, i) overall cross-sectional morphologies; (a1, c1, e1, g1, i1) magnified views of the interaction region; (b, d, f, h, j) corresponding elemental distributions.

In summary, the biomimetic multilayer coating forms multiphase reaction products *in situ* via a dissolution–reprecipitation mechanism during high-temperature corrosion, thereby progressively constructing a stable composite barrier. The corrosion mechanism transitioned from an initial rapid-reaction stage to a diffusion-controlled stage, significantly enhancing the resistance of the coating to corrosion from the molten environment. This successful mechanism highlights the synergy

Table 8 Elemental compositions (at%) of points indicated in Fig. 13

Sample		Composition (at%)													Phase
		Si	Ca	Na	Al	Mg	K	Ti	Fe	Y	Yb	Gd	Zr	O	
1400 °C, 20 h	G1	28.9	0.6	1.3	3.9	0.4	1.1	0.2	0.1	—	—	—	—	63.6	Melt
	G2	20.0	—	—	—	—	—	—	—	11.5	2.9	2.0	—	63.7	Silicate
	G3	15.2	2.8	—	—	—	—	—	—	16.3	2.9	3.2	—	59.7	Apatite
	G4	4.4	0.8	—	—	—	—	—	—	9.4	2.1	1.9	16.0	65.4	Fluorite + apatite
1400 °C, 50 h	G5	35.2	0.6	1.3	4.2	0.4	1.3	0.0	0.1	—	—	—	—	56.9	Melt
	G6	24.1	—	—	—	—	—	—	—	14.3	3.7	2.3	—	55.6	Silicate
	G7	17.2	3.0	—	—	—	—	—	—	17.8	3.0	3.5	—	55.5	Apatite
	G8	2.2	—	—	—	—	—	—	—	19.6	3.3	3.4	18.0	53.6	Fluorite
	G9	16.9	2.4	—	—	—	—	—	—	18.1	2.6	3.9	—	56.2	Apatite
1400 °C, 100 h	G10	29.8	0.4	1.4	4.1	0.2	1.2	0.0	0.2	—	—	—	—	62.8	Melt
	G11	18.7	—	—	—	—	—	—	—	13.1	2.4	2.3	—	63.5	Silicate
	G12	14.4	1.6	—	—	—	—	—	—	16.8	2.5	3.3	—	61.4	Apatite
	G13	3.4	—	—	—	—	—	—	—	10.6	2.4	2.6	19.5	61.6	Fluorite
	G14	10.7	1.3	—	—	—	—	—	—	16.6	3.4	2.9	—	65.1	Apatite

between material chemistry and structural design: its superior corrosion resistance is attributed primarily to the excellent chemical reactivity of the YYbGdZO top layer, which precludes the infiltration-driven failure mode observed in the MRE-SZ/YSZ system by rapidly forming a dynamic barrier at the surface. Concurrently, the MRE-SZ transition layer is crucial for mitigating interlayer property mismatches and ensuring long-term structural stability. Thus, the three-layer graded design in this study highlights the synergistic advantage of combining the "chemical defense" of the top layer with the "structural robustness" provided by the transition layer.

3.5.3 In situ self-generated reactions of the YYbGdZO layer against CMAS-E attack

To further elucidate the intrinsic mechanism behind the superior corrosion resistance of the biomimetic multilayer coating, the microstructure and elemental distribution of the cross section of a sample corroded for 20 h were characterized via EPMA. As shown in Fig. 14(a), after 20 h of high-temperature corrosion, the corrosive effects were entirely confined within the top YYbGdZO layer, whereas the underlying MRE-SZ and YSZ functional layers remained structurally intact and uncorroded. This provides initial validation for the effectiveness of the YYbGdZO layer's design as a "sacrificial" dynamic response layer.

Figure 15(a) presents a high-magnification micrograph of the reaction zone, revealing its intricate internal defensive structure in greater detail. A reaction layer, approximately 10.8±0.9 μm thick, formed *in situ* at the interface with the residual CMAS-E melt. Notably, the original intersplat pores beneath this barrier are filled with new reaction products (primarily apatite), revealing a crucial "internal self-sealing" mechanism. This phenomenon provides compelling evidence that the small amount of melt that infiltrated before the main barrier was fully established continuously reacts *in situ* with the pore walls until its active components are consumed and converted into thermodynamically stable solid ceramic phases. This process, which transforms a fluid, corrosive melt into a solid filler, not only effectively prevents its further deep infiltration but also mitigates the potential risk of stress generation during thermal cycling due to phase changes or thermal mismatch, thereby significantly increasing the robustness of the entire defense system.

This successful defense mechanism stands in stark contrast to the failure mode of the MRE-SZ/YSZ coating, offering a key perspective to elucidate its buckling mechanism. To present this difference more directly, Table 9 summarizes the key performance comparisons between the two coatings after CMAS-E corrosion. The significant performance disparity presented in Table 9 stems from the fundamentally different thermomechanical coupled failure/defense mechanisms of the two systems. The failure of MRE-SZ is a thermomechanical coupled process involving the degradation of the entire coating thickness. Owing to its insufficient reactivity, the CMAS-E melt infiltrates deeply, creating a heterogeneous microstructure within the MRE-SZ layer: the top region becomes dense and brittle from zircon precipitation, whereas the interior is densified by melt-filled pores. This transformation, characterized by "surface embrittlement" and "internal densification", fundamentally destroys the original high strain tolerance of the coating. Consequently, during cooling, the immense in-plane compressive stresses generated by the significant coefficient of thermal expansion (CTE) mismatch between this modified, dense layer and the underlying YSZ layer cannot be effectively accommodated, ultimately leading to catastrophic failure by buckling and delamination. Conversely, the dynamic defense mechanism of YYbGdZO successfully confines corrosion to a beneficial "surface effect". Its high reactivity limits the corrosion-affected zone to a very thin surface layer. This strategy sacrifices the strain tolerance of a minimal volume to protect the integrity and porosity of the entire underlying bulk structure, ultimately preserving the macroscopic stress-releasing capability of the coating. Consequently, the thermal mismatch stresses generated during cooling are much smaller than those in the MRE-SZ system and can be effectively accommodated and dissipated by the intact, highly strain-tolerant porous structure underneath, thereby effectively averting the onset of buckling.

Through detailed elemental mapping of this region (Figs. 14(b)–14(m) and 15(b)–15(m)), the critical roles of the different RE elements in constructing this dynamic defense barrier and their synergistic mechanisms can be elucidated. As shown in Fig. 15(b), Si is predominantly enriched at the outermost edge of the dense barrier layer. Correspondingly, the RE elements Y, Yb, and Gd (Figs. 15(c), 15(e), and 15(f)) also exhibit high concentrations in this region. This indicates that the multicomponent RE ions from the coating rapidly reacted with the SiO_2 from the melt to form a continuous RE silicate layer at the solid/liquid interface. This layer

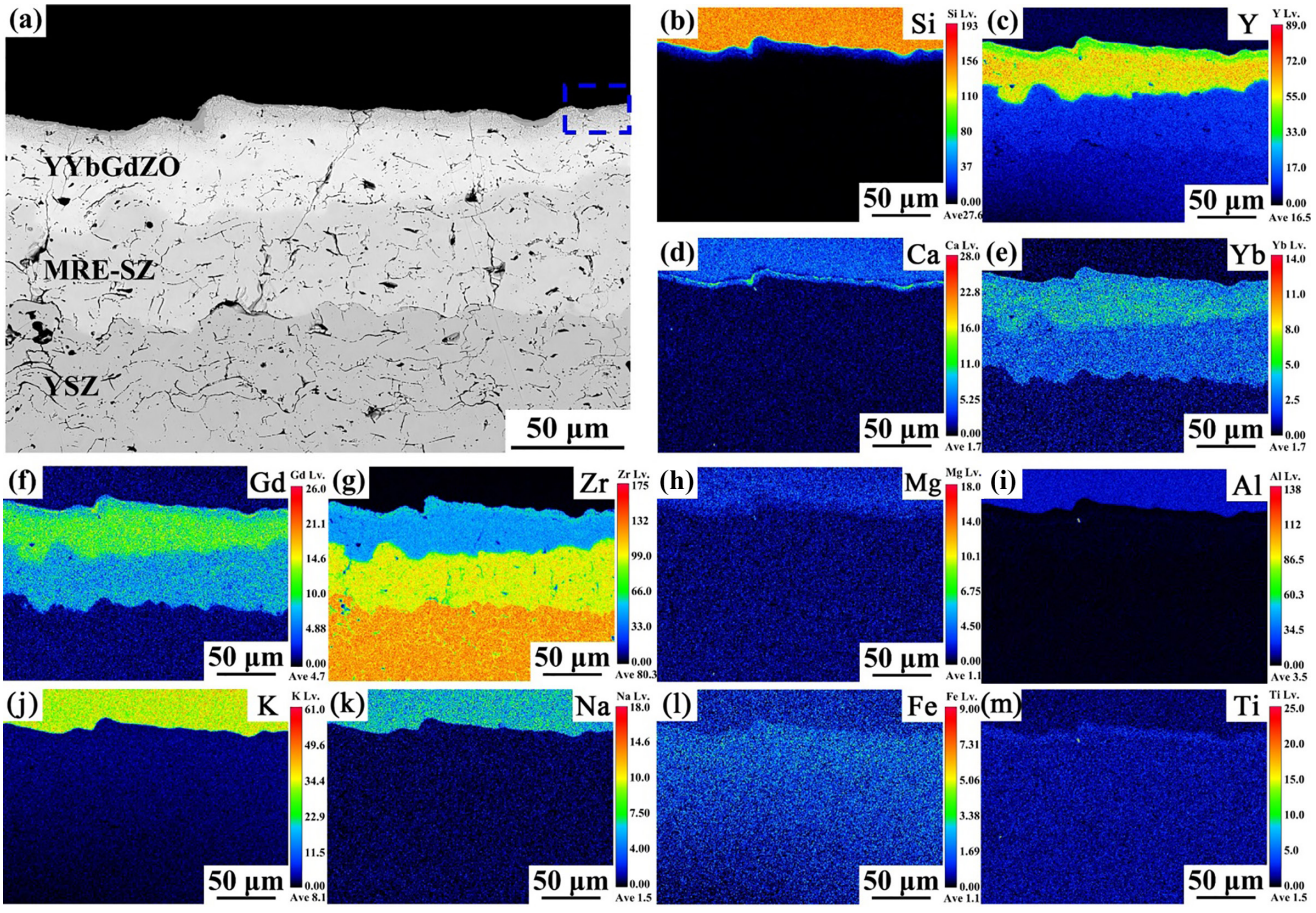

Fig. 14 Microstructural features and elemental distributions of bioinspired multilayer coating after exposure to CMAS-E at 1400 °C for 20 h: (a) cross-sectional microstructure and (b–m) corresponding elemental distribution maps.

serves as the first physical barrier, effectively isolating the bulk of the melt. Of particular importance is the phase evolution on the inner side of the reaction layer. The elemental maps (Figs. 15(d), 15(h), and 15(k)) clearly show that Ca, Mg, and a small amount of Na did not remain at the outermost surface but instead formed a distinct and well-defined coenrichment zone beneath the RE silicate layer. This enriched zone shows a high degree of overlap with the distributions of Gd and Y, providing strong evidence for the formation of a complex, multielement apatite solid solution. This process profoundly demonstrates the superiority of multicomponent RE design. The apatite crystal structure is highly flexible, with cation lattice sites capable of accommodating a variety of ions with different radii and valence states. In this system, RE elements with larger ionic radii (especially Gd^{3+}), which are similar in size to Ca^{2+}, have a strong thermodynamic driving force to form the apatite phase [5,30,52]. During the reaction, the chemically active Ca^{2+} ions from the melt are consumed in large quantities and immobilized within the stable apatite lattice. Concurrently, more mobile cations such as Mg^{2+} and Na^{+} are also incorporated into the lattice, leading to the *in situ* formation of a compositionally complex $(Ca,Mg,Na,RE)_{10}(SiO_4)_6O_2$ apatite phase, where RE represents a combination of Gd and Y. The formation of this multielement solid solution achieves the simultaneous consumption and fixation of various active cations from the melt. This, in turn, fundamentally alters the chemical nature of the residual melt, significantly reducing its overall corrosivity and achieving deep chemical passivation of CMAS-E. Throughout the entire reaction zone, Zr (Fig. 15(g)) is co-distributed with RE elements, forming a stable, reprecipitated c-ZrO_2 phase. These c-ZrO_2 phases, combined with apatite and RE silicates, constitute the robust skeleton of the dense barrier, further enhancing its physical blockade capability and structural stability.

The formation of this functional, multiphase barrier stands in stark contrast to the reaction pathway in the MRE-SZ system, where zircon is the primary product. This difference is rooted in the distinct kinetic competition that arises when the intrinsic chemical composition of each coating interacts with the Si-rich CMAS-E melt. In the MRE-SZ system, which has a relatively low RE^{3+} ion concentration, the extremely low solubility of Zr^{4+} in the silicate melt becomes the dominant factor. Consequently, when the Si-rich melt contacts the coating, the interface first becomes supersaturated with respect to Zr^{4+}, kinetically driving the preferential precipitation of zircon $ZrSiO_4$. Conversely, the very high RE^{3+} ion concentration and high reactivity of the YYbGdZO system lead to simultaneous enrichment of both RE^{3+} and Si^{4+} ions at the interface upon contact with the Si-rich melt. This creates highly favorable conditions for the nucleation of RE silicates, making them the dominant reaction pathway. Therefore, the YYbGdZO system, through its sophisticated compositional design, actively regulates the relative concentrations and saturation levels of reactants at the interface, thereby steering the reaction pathway toward the construction of a functional, multilayered barrier and avoiding the formation of the single, nonprotective product seen in the MRE-SZ system.

In summary, the YYbGdZO dynamic response layer, through its unique multicomponent RE composition, undergoes a highly efficient and well-stratified *in situ* reaction with the CMAS-E melt. This reaction synergistically forms a multilayered, highly effective dynamic defense barrier that integrates a "dual physical blockade"

(a dense RE silicate layer + apatite pore-sealing) with "chemical passivation" (apatite phase), thereby providing the entire coating system with long-lasting corrosion protection.

To quantitatively evaluate the protective efficiency of the *in situ* self-generated reaction barrier and elucidate its growth mechanism, a kinetic analysis of the infiltration depth and the equivalent thickness of each phase within the reaction zone was conducted as a function of time. The results are presented in Fig. 16. Figure 16(a) shows the relationship between the total reaction zone depth and the corrosion time. The reaction depth clearly increases rapidly in the initial stage of corrosion (0–5 h), after which the growth rate decreases significantly. This nonlinear growth trend provides a preliminary indication that the corrosion process is not controlled by a constant-rate interfacial reaction but is more likely limited by the diffusion of ions through the progressively thickening product layer. To further verify this inference, the growth kinetics of the primary reaction products (RE silicate, apatite, and fluorite phases) were fitted via the classic parabolic rate model ($x^2 = k_p t$, or its equivalent, $x = k_p t^{1/2}$, where k_p is the parabolic rate constant). As shown in Fig. 16(b), the equivalent thickness (x) of each phase was plotted against the square root of the corrosion time ($t^{1/2}$). The results show that the equivalent thicknesses of the RE silicate, apatite, and fluorite phases all exhibit excellent linear relationships with $t^{1/2}$, with high coefficients of determination (R^2) of 0.985, 0.999, and 0.993, respectively. This finding provides compelling evidence that the growth kinetics of the *in situ* reaction product layer strictly follow a parabolic law, which is characteristic of a diffusion-controlled mechanism. The physical significance is that the phases generated from the reaction between the YYbGdZO coating and the CMAS-E melt are dense and collectively form an effective ion diffusion barrier. As this barrier thickens, the diffusion paths for corrosive

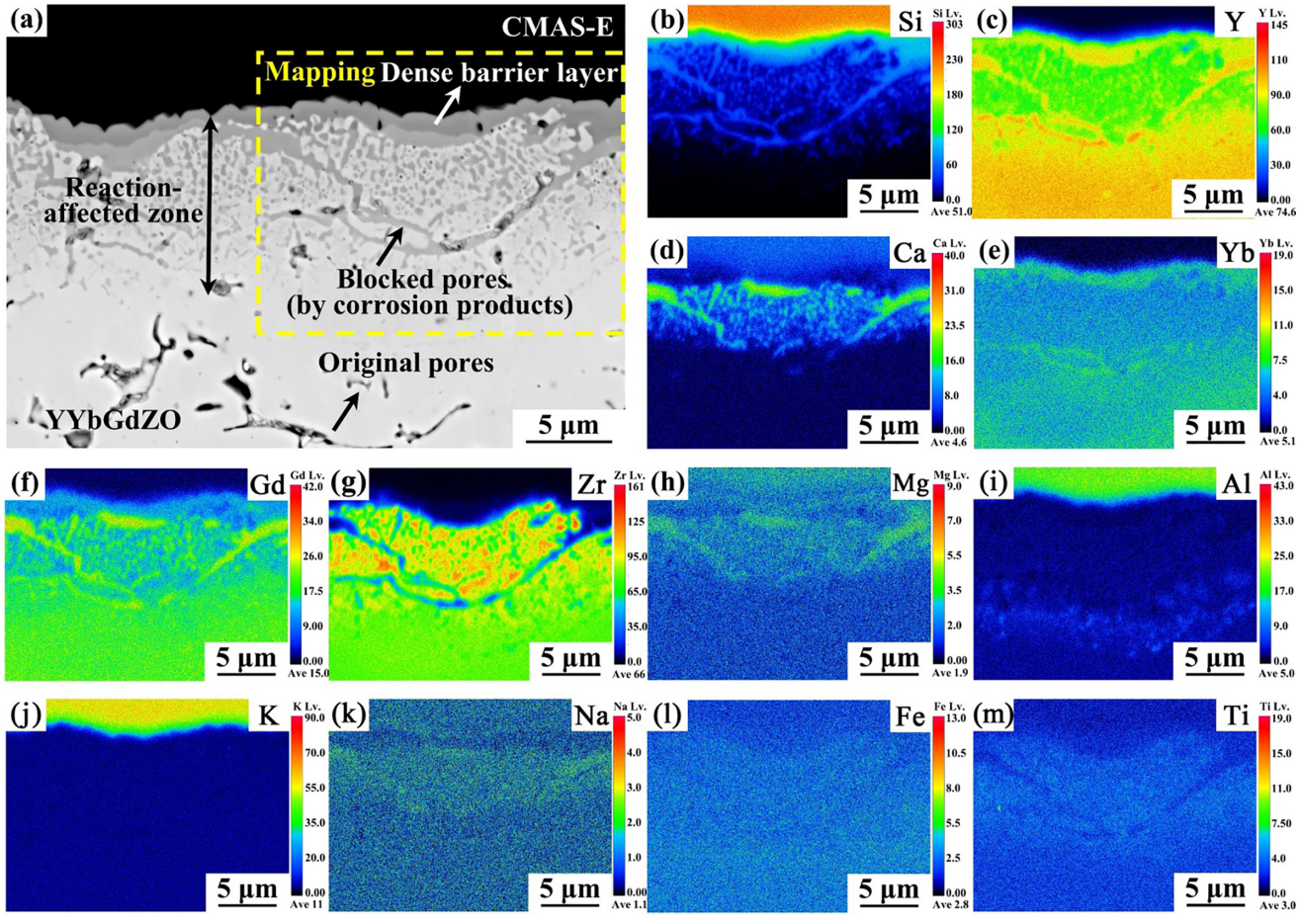

Fig. 15 High-magnification microstructural features of YYbGdZO top layer after exposure to CMAS-E at 1400 °C for 20 h (corresponding to blue rectangle in Fig. 14) and associated elemental distributions: (a) cross-sectional microstructure showing a dense barrier layer, blocked pores, and reaction-affected zone; (b–m) corresponding elemental distribution maps.

Table 9 Comparison of performance characteristics of biomimetic multilayer coating and MRE-SZ/YSZ coating after CMAS-E corrosion at 1400 °C

Coating	MRE-SZ/YSZ	Biomimetic multilayer coating
Corrosion duration (h)	50	100
Final state	Failed	Intact
Primary failure mode	Buckling and delamination	Structurally intact, no buckling failure observed
Maximum penetration depth	Full penetration through MRE-SZ layer	18.8±1.5 μm
Primary reaction products	Zircon and c-ZrO_2	RE silicate, apatite, and fluorite
Protective mechanism	No continuous barrier formed	Dense, multilayered barrier formed *in situ*

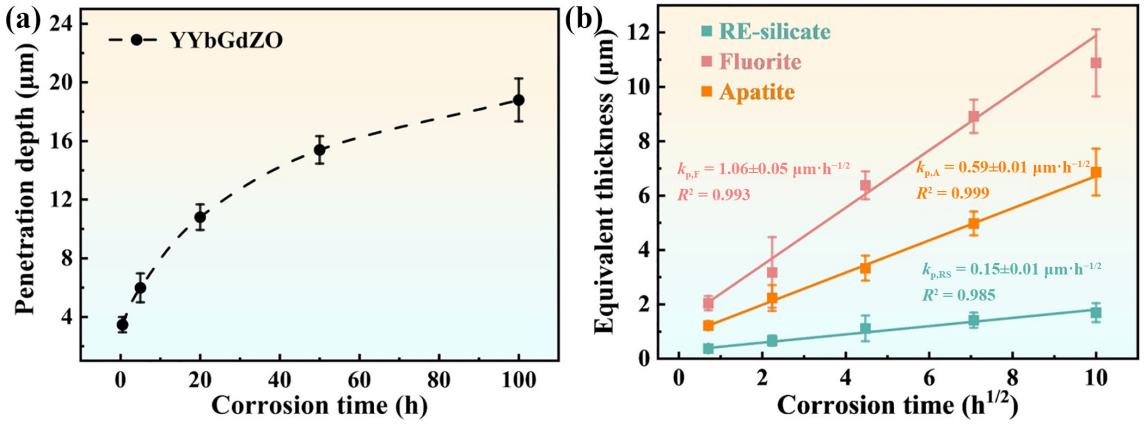

Fig. 16 Penetration depth of YYbGdZO layer and parabolic growth of reaction products at 1400 °C: (a) reaction zone depth vs. corrosion time and (b) equivalent thickness of different phases vs. square root of corrosion time.

ions (e.g., Ca^{2+} and Mg^{2+}) from the melt and for RE ions from the coating outward become longer and more tortuous, leading to a significant reduction in the overall reaction rate.

A comparison of the parabolic growth rate constants reveals that the equivalent growth rate of the fluorite phase is the highest ($k_{p,F}$ = 1.06±0.05 μm·h$^{-1/2}$), followed by the apatite phase ($k_{p,A}$ = 0.59±0.01 μm·h$^{-1/2}$), and finally the RE silicate phase ($k_{p,RS}$ = 0.15±0.01 μm·h$^{-1/2}$), i.e., $k_{p,F} > k_{p,A} > k_{p,RS}$. This kinetic sequence provides profound insight into the complex and highly efficient synergistic mechanism within the biomimetic defense barrier. First, the fastest growth rate belongs to the $k_{p,F}$ (c-ZrO_2). The increase in its equivalent thickness essentially represents the expansion of the RE-depleted zone, formed by the preferential outward diffusion of RE^{3+} ions. This indicates that the release of RE^{3+} ions—the "raw material" for subsequent reactions—from the YYbGdZO matrix is a kinetically rapid process. Thus, $k_{p,F}$ can be considered a direct indicator of the intrinsic reactivity of the YYbGdZO coating. This high-speed "sacrificial" diffusion provides an ample material basis for the rapid construction of protective layers. Second, the growth rate of the $k_{p,A}$ is intermediate. Its formation depends on the meeting of outward-diffusing RE^{3+} ions from the matrix and inward-diffusing ions such as Ca^{2+} from the melt. Its key role is the chemical passivation of the melt by consuming the most chemically active Ca^{2+} ions and incorporating impurities, which fundamentally reduces the melt's corrosivity. Finally, the $k_{p,RS}$ has the slowest growth rate. This phenomenon, while seemingly counterintuitive given the layer's outermost position, is governed by complex ion transport dynamics. The thickening of the barrier involves both the outward diffusion of RE^{3+} ions and the inward diffusion of Ca^{2+}/Si^{4+} ions. The faster growth of the inner apatite/fluorite zone indicates that the inward flux of Ca^{2+}/Si^{4+} ions is greater than the outward flux of RE^{3+} ions reaching the final reaction front. This can be attributed to a potentially higher effective diffusion coefficient for Ca^{2+}/Si^{4+} through the nascent reaction layer and a steeper concentration gradient provided by the "infinite source" of the melt. Consequently, the growth of the outermost RE silicate layer is kinetically limited by the relatively slow "supply" of RE^{3+} ions, becoming the rate-limiting step for the overall reaction. This slowest step ultimately governs the long-term stability and superior protective performance of the entire barrier system. This mechanism also explains the spatial ordering of the layers: RE silicate forms preferentially at the outermost interface with high Si^{4+} and RE^{3+} concentrations, whereas apatite forms in the inner region where inward-diffusing Ca^{2+} meets outward-diffusing RE^{3+}.

In summary, the kinetic analysis results are in excellent agreement with the microstructural observations, collectively revealing the dynamic defense mechanism of the biomimetic coating: an initial rapid reaction quickly results in a composite barrier with both physical blockade and chemical passivation functions. The corrosion process subsequently transitions to a stage controlled by the slow diffusion of ions through this barrier. This multiphase, multilayered synergistic growth dynamic endows the coating system with exceptional and long-lasting resistance to CMAS-E corrosion.

3.6 CMAS-E corrosion resistance mechanism of bioinspired multilayer coatings: *in situ* dynamic defense barrier

3.6.1 Mechanisms of surface morphology-driven preferential apatite nucleation

A key phenomenon observed in the preceding microstructural evolution analysis is the preferential growth behavior of apatite. During the initial stage of corrosion, the apatite reaction product preferentially nucleates and grows in the surface depressions and pores of the YYbGdZO coating, whereas its formation is hindered on protruding asperities. As the reaction proceeds, these preferentially nucleated crystals grow and coalesce, eventually evolving into a continuous and dense protective layer. This phenomenon indicates that the inherent surface roughness of the APS coating not only alters the local reaction environment but also plays a critical regulatory role in the formation and evolution of the dynamic defense barrier. As shown by the comparative experimental results, the as-sprayed and surface-polished YYbGdZO coatings exhibit significant differences after reacting with the CMAS-E melt for 30 min at 1400 °C (Fig. 4). Specifically, when the molten CMAS-E contacts the original rough surface, the wetting behavior is nonuniform at the microscale. This is attributed to the different contact angles (θ) of the liquids in the concave and convex regions. This variation in contact angle not only causes differences in melt wetting on surfaces with varying curvatures but also influences the free energy barrier for heterogeneous nucleation by modulating the local degree of wetting.

This preferential nucleation of the apatite phase within the reaction layer can be explained by classical heterogeneous nucleation theory [53,54]. The energy barrier for heterogeneous nucleation (i.e., nucleation at the substrate/melt interface), ΔG^*_{hetero}, is determined by Eqs. (1) and (2):

$$\Delta G^*_{hetero} = \frac{16}{3}\frac{\pi\gamma_{sl}^3\Omega^2}{k^2T^2\ln^2(1+\sigma)} \times f(\beta,\theta) \quad (1)$$

$$f(\beta,\theta)=\frac{1}{4}\left(2-3\sin\left(\frac{\beta}{2}+\theta\right)+\sin^3\left(\frac{\beta}{2}+\theta\right)-\cos^3\left(\frac{\beta}{2}+\theta\right)\cot\frac{\beta}{2}\right) \quad (2)$$

where θ is the contact angle of the nucleus on the substrate, β is the cone angle, γ_{sl} is the interfacial energy between the crystal surface and the supersaturated solution, Ω is the monomer volume of the nucleus, k is the Boltzmann constant, T is the temperature, and σ is the supersaturation.

Aside from the constant terms determined by the material and environment, the critical term is the heterogeneous nucleation factor, $f(\theta,\beta)$. This factor, which describes the reduction in the nucleation energy barrier relative to that of homogeneous nucleation, is strongly dependent not only on the intrinsic θ between the new phase nucleus and the substrate but also on the local geometry of the substrate surface, described here by β. For a rough surface, concave regions/pores have a concave geometry with an equivalent $\beta > 180°$; flat regions can be considered $\beta = 180°$; and convex regions have a convex geometry with $\beta < 180°$.

Theoretical studies have demonstrated that the value of the $f(\theta,\beta)$ decreases as the β increases. This means that, all other conditions being equal, the magnitude of the nucleation energy barrier (ΔG^*_{hetero}) follows the order of concave regions < flat regions < convex regions. Therefore, from a thermodynamic standpoint, the nuclei of the new phase form most readily in the surface depressions. This surface geometry-driven preferential nucleation of apatite is intuitively illustrated in the schematic in Fig. 17. As shown, the nucleation of the apatite phase is "easiest" in regions with a concave geometry ($\beta > 180°$), making these areas preferential reaction sites. Once nucleated, the crystals begin to grow and expand outward, gradually covering the regions where nucleation is moderately difficult (flat regions, $\beta = 180°$) and most difficult (convex regions, $\beta < 180°$). Ultimately, the crystalline products originating from different concave regions coalesce, synergistically forming a continuous protective layer. The concave regions and pores are not only the first sites to be occupied by the melt but also provide a larger solid/liquid reaction interface and a relatively confined microenvironment. After the RE ions (Y^{3+}, Yb^{3+}, and Gd^{3+}) from the coating dissolve into the melt, this geometric confinement allows the local ion concentration to rapidly reach the supersaturation (σ) required for apatite formation, thereby promoting its preferential and rapid precipitation. In contrast, for the protruding "peaks", the positive curvature increases the effective contact angle, inhibiting the spreading of the melt. Furthermore, the positive curvature makes heterogeneous nucleation thermodynamically more difficult, requiring it to be initiated at surface defects or high-energy sites. This explains the observation that in the early stages of corrosion evolution (Figs. 6(c), 13(c1), and 15(a)), the apatite phase is predominantly formed in pores and surface depressions.

In stark contrast is the polished smooth surface (Fig. 4(e)). Ideally, the solid/liquid contact line on a flat plane can be approximated as 180°, and the wetting behavior is relatively simple, lacking the local energy variations introduced by geometric roughness. Therefore, compared with a rough surface with convex and concave features, heterogeneous nucleation on a smooth interface is of intermediate thermodynamic difficulty. However, because the coating still contains a network of pores and defects, these features lower the nucleation energy barrier to some extent, allowing nucleation to occur readily. The experimental results (Figs. 4(f) and 6(e)) show that a relatively uniform layer of reaction products formed on the polished surface, in which the apatite phase exhibited a unique "rod-bundle" morphology. This finding indicates that in the absence of roughness-induced preferential/delayed nucleation sites, the growth rate of the reaction products can exceed the macroscopic wetting and spreading rates of the melt. Once the reaction is initiated, the resulting solid layer rapidly "pins" the three-phase contact line, inhibiting further lateral spreading of the melt and causing the interfacial evolution to be dominated by growth perpendicular to the interface.

In summary, the surface roughness of the APS coating effectively lowers the heterogeneous nucleation energy barrier by modulating the local topography, causing key products such as apatite to form preferentially in pores and depressions, thereby sealing the infiltration pathways first. This "morphology-driven" preferential nucleation mechanism significantly accelerates the construction of the barrier layer and is a core foundation for the active, dynamic defense characteristics of the coating.

3.6.2 *Mechanisms of the in situ formation of a dynamic defense barrier*

The collective results of this study reveal a highly effective "*in situ*

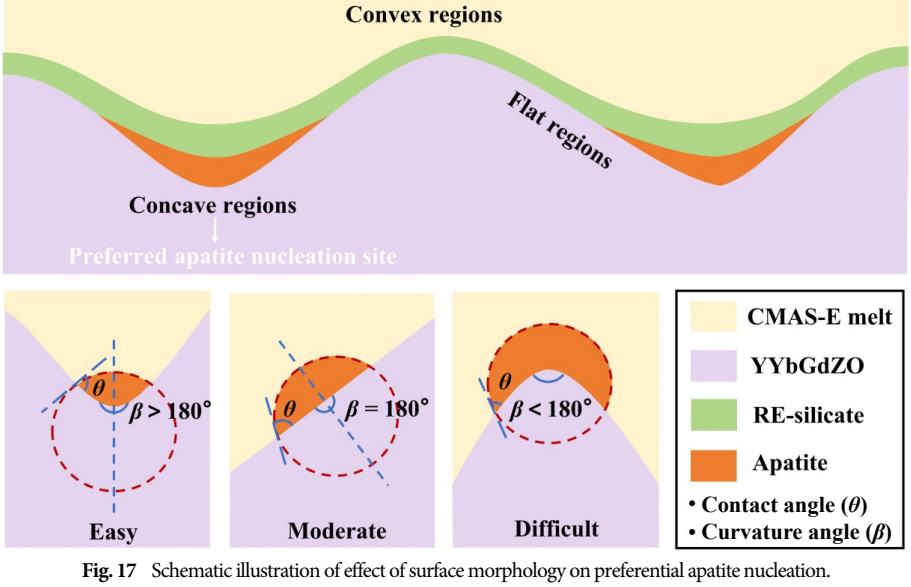

Fig. 17 Schematic illustration of effect of surface morphology on preferential apatite nucleation.

dynamic defense" mechanism against corrosion, inspired by the natural process of pearl formation. The core of this mechanism is the ability of the biomimetic multilayer coating to actively respond to the corrosive attack of complex CMAS-E melts by forming, *in situ*, a multilayered, multiphase composite barrier that provides both physical blockade and chemical passivation. This "stimulus-response" behavior functionally mimics the adaptive defense process of nacre encapsulating and neutralizing foreign objects, endowing the coating with a protective ability that far exceeds that of conventional materials. The advantage of this design, compared with the passive dissolution of traditional YSZ or single-reactive materials, lies in its dynamic, multifaceted, and self-adaptive barrier construction. The complete mechanism is systematically illustrated in Fig. 18. The formation of a dynamic self-generating barrier is a dynamic, multistage evolutionary process. This process can be summarized in three interconnected stages:

In Stage 1, the molten CMAS-E, owing to its fluidity, begins to infiltrate through rapid infiltration channels, such as the inherent interlamellar porosity and columnar grain boundaries of the APS coating. The high intrinsic reactivity of the YYbGdZO material prevents the molten CMAS-E from just penetrating directly, instead triggering a vigorous dissolution–precipitation reaction upon surface contact. The YYbGdZO coating underwent interface dissolution, continuously releasing multiple RE ions (Y^{3+}, Yb^{3+}, and Gd^{3+}) and Zr^{4+} ions into the melt.

In Stage 2, as dissolution progresses, a complex crystallization process, which is controlled by both thermodynamics and kinetics, begins. Experimental observations show that apatite preferentially nucleates at surface depressions and interlayer pores in the coating. This is not coincidental but rather the result of kinetic limitations imposed by the supply of reactants and the thermodynamic advantage of nucleating at rough surfaces. From a kinetic perspective, the formation of apatite is limited by the low concentration of one of its key reactants, Ca^{2+}, in the CMAS-E melt (the CaO content is only 3.17 wt%). The scarcity of this reactant strongly limits mass transport, causing the chemical

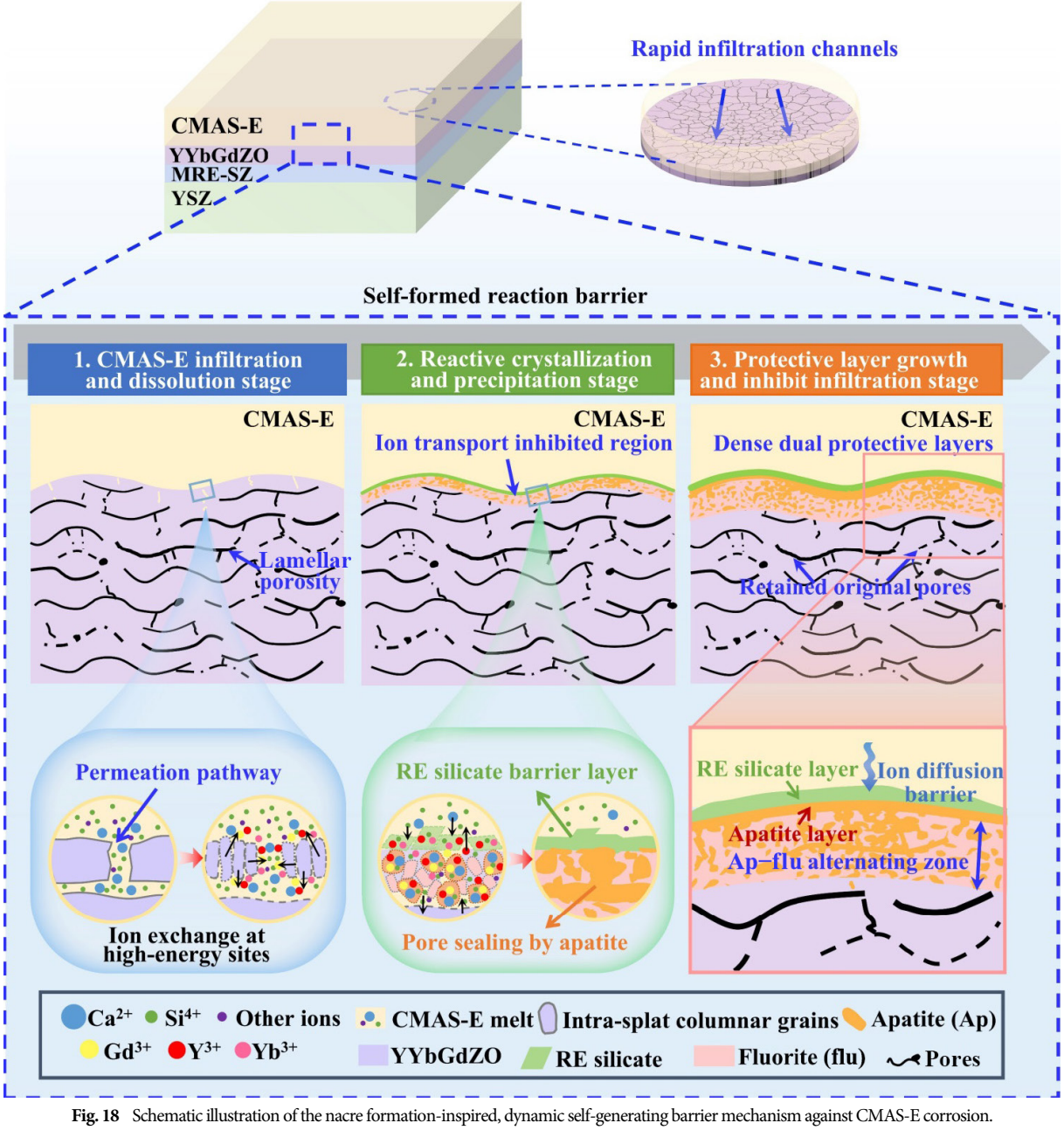

Fig. 18 Schematic illustration of the nacre formation-inspired, dynamic self-generating barrier mechanism against CMAS-E corrosion.

reaction to favor sites that minimize the activation energy. From a thermodynamic perspective, nucleation occurs at the lowest energy barrier, which is found in recessed areas such as pores or crack tips, rather than flat or protruding surfaces. Therefore, the preferential nucleation of apatite can be understood as a search for the most thermodynamically favorable "shortcut". The natural pits and interlayer pores on the atmospheric plasma-sprayed coating surface provide these low-energy nucleation sites, facilitating the preferential formation of apatite even under extremely low Ca^{2+} concentrations, thereby selectively blocking the infiltration channels. In contrast to the conditions required for apatite formation, the formation of the outer RE silicate $(Y,Yb,Gd)_2Si_2O_7$ occurs under conditions of abundant reactants. On the one hand, the CMAS-E melt contains a very high concentration of SiO_2 (approximately 79.86 wt%), and on the other hand, the top layer of YYbGdZO continuously provides RE ions (Y^{3+}, Yb^{3+}, and Gd^{3+}) to the reaction interface under high-temperature conditions. With sufficient reactants available, the reaction no longer depends on finding specific low-energy nucleation sites. Instead, as long as the solid–liquid interface satisfies basic reaction conditions, the smaller ions in YYbGdZO (Y^{3+}, Yb^{3+}) preferentially and rapidly diffuse to the outermost solid–liquid interface, reacting with the SiO_2 enriched in the molten material to rapidly form a continuous, dense $(Y,Yb,Gd)_2Si_2O_7$ crystalline layer. Therefore, the formation of RE silicates manifests macroscopically as a continuous, dense "blanket" layer over the entire coating–melt interface without exhibiting significant preferential nucleation characteristics.

Stage 3 is the barrier thickening and stabilization phase. As corrosion progresses, the initial crystalline products grow and interconnect, ultimately forming a continuous, dense composite defense barrier on the coating surface. The final dynamic self-generating barrier structure reflects the clear functional division of multielement RE ions on the basis of their inherent properties. The smaller ions Y^{3+} (1.019 Å, CN = 8) and Yb^{3+} (0.985 Å, CN = 8) in YYbGdZO [55,56] preferentially and rapidly diffuse to the outermost solid–liquid interface, reacting with the SiO_2 in the molten material to rapidly form a continuous, dense $(Y,Yb,Gd)_2Si_2O_7$ crystalline layer. This layer serves as the first physical barrier, effectively isolating the molten material from macroscopic erosion. Although its initial formation is rapid, kinetic analysis revealed that its subsequent thickening process (growth rate) is the slowest. This is due to the long-range diffusion of RE^{3+} ions, which must traverse the entire thickening internal reaction layer. This longest ion migration path creates the major kinetic barrier, making the layer stable and durable. Beneath the RE silicate layer lies the apatite layer and apatite/fluorite composite layer. The formation of this layer is a result of both thermodynamic selectivity and ion size compatibility. The larger Gd^{3+} ions (1.053 Å, CN = 8) in YYbGdZO and Ca^{2+} ions (1.12 Å, CN = 8) in the molten material have similar ion radii (a difference of approximately 6%) [55,57], providing good compatibility in the crystal structure and creating a strong thermodynamic drive to promote their coprecipitation as apatite. Additionally, medium-sized Y^{3+} ions also participate in apatite formation, which is consistent with reports that Y ions can stabilize within the apatite lattice. This layer plays a dual key role. First, the complex apatite phase formed by Gd and Y consumes highly mobile and chemically active ions such as Ca^{2+} and Mg^{2+} from the melt [58], achieving chemical passivation of the molten material. Second, apatite and the reprecipitated fluorite phases together form a biomimetic microstructure that is structurally analogous to the "brick-and-mortar" architecture of nacre. However, whereas in natural nacre, this structure provides mechanical toughness via a flexible phase, its primary function here is different: it creates a highly convoluted, labyrinth-like pathway. This tortuous path significantly increases the diffusion path length for corrosive ions (such as Ca^{2+} and Mg^{2+}), forming an efficient ion diffusion barrier and imparting excellent structural stability and resistance to permeation at the reaction interface.

The full establishment of this multifunctional composite barrier, which integrates physical isolation, chemical passivation, and ion diffusion suppression, marks a critical transition in the corrosion mechanism. The corrosion process successfully shifts from an initial stage of rapid reaction and infiltration to a stable stage controlled by slow ion diffusion within the dense layer, following a parabolic law. Even after 100 h of severe corrosion (Fig. 13(i)), the barrier remains structurally stable, effectively containing corrosion within the YYbGdZO top layer, whereas the underlying MRE-SZ and YSZ functional layers remain intact, providing long-lasting and stable protection.

In summary, by functionally mimicking the adaptive defense mechanism of a pearl, the biomimetic multilayer coating transforms the "invasive stimulus" of CMAS-E into the "driving force" for constructing its own protective layer, successfully achieving an "*in situ* dynamic response" against complex CMAS-E melt attack. Through a three-stage process of "rapid responsive sealing, synergistic barrier construction, and final transition to diffusion control", the coating generates, *in situ*, a multifunctional composite barrier that integrates physical blockade, chemical passivation, and ion diffusion suppression, thereby providing the TBC system with exceptional and long-lasting corrosion protection.

4 Conclusions

Inspired by the adaptive defense mechanism of nacre formation, this study proposes and fabricates a novel YYbGdZO/MRE-SZ/YSZ multilayer TBC capable of a biomimetic "self-response" defense. After 100 h of severe corrosion at 1400 °C at a low Ca/Si ratio, the impurity-containing CMAS-E coating demonstrated high durability, with corrosion confined effectively within the top layer, forming a reaction layer of only 18.8±1.5 μm while avoiding the buckling failure mode.

The core of this resistance lies in the highly reactive YYbGdZO top layer, which actively reacts with the CMAS-E melt to construct an *in situ* multifunctional dynamic self-generating barrier, a mechanism that is particularly superior in low-Ca/Si-ratio environments where traditional apatite-based protection is limited. This barrier, composed of an outer continuous RE silicate layer and an inner apatite/fluorite composite that is structurally analogous to a nacre-like "brick-and-mortar" architecture, synergistically achieves a triple defense of "physical blockade" "chemical passivation" and "ion diffusion suppression".

The ordered construction of this barrier is a profound manifestation of synergistic chemical and physical control. The chemical synergy arises from a clear functional division of labor among the RE ions dictated by their intrinsic properties, wherein smaller ions such as Y^{3+} and Yb^{3+} dominate the formation of the outer physical shield, whereas the larger Gd^{3+} ion is crucial for constructing the inner chemical passivation layer. The physical synergy is expressed through a dual-sealing mechanism, where the outer RE silicate layer forms a continuous macroscopic shield, whereas the inner apatite phase, which is thermodynamically guided by the coating microstructure, preferentially nucleates within pores and depressions to seal critical microscopic infiltration channels.

Kinetic analysis indicates that the corrosion process follows a

"rapid formation, slow thickening" parabolic law. The formation of the dynamic self-generating barrier rapidly transitions the corrosion mechanism from an initial stage of reaction and infiltration into one controlled by slow ion diffusion, wherein the slow growth of the outermost RE silicate layer ($k_{p,RS}$ = 0.15± 0.01 μm·h$^{-1/2}$) ensures long-term protection.

In summary, the nacre formation-inspired, dynamic self-generating barrier mechanism elucidated in this work, which transforms a corrosive attack into the driving force for its own protection, offers a new design paradigm for developing next-generation TBCs with long-term durability and high reliability against environmental deposit corrosion.

Acknowledgements

This work was supported by the National Natural Science Foundation of China (Nos. 52471092 and 52301102), the Postdoctoral Research Foundation of China (No. 2024M752571), and the Fundamental Research Funds for the Central Universities.

Author contributions

Yao-Xu Zan: conceptualization, data curation, formal analysis, investigation, methodology, software, writing—original draft. Lu-Huang: data curation, formal analysis, investigation. Wei-Zheng Gu: investigation, writing—review & editing. Peng-Shuai Yue: investigation, writing—review & editing. Lin Dong: resources, supervision, validation funding acquisition. Mei-Jun Liu: conceptualization, methodology, funding acquisition, resources, supervision, writing—review & editing. Guan-Jun Yang: conceptualization, funding acquisition, resources, supervision.

Availability of data and materials

The data that support the findings of this study are available from the corresponding author upon reasonable request.

Competing interests

The authors have no competing interests to declare that are relevant to the content of this article. The author Guan-Jun Yang is the Editorial Committee member of this journal.

References

[1] Clarke DR, Oechsner M, Padture NP. Thermal-barrier coatings for more efficient gas-turbine engines. *MRS Bull* 2012, **37**: 891–898.

[2] Miller RA. Current status of thermal barrier coatings—An overview. *Surf Coat Tech* 1987, **30**: 1–11.

[3] Padture NP. Advanced structural ceramics in aerospace propulsion. *Nat Mater* 2016, **15**: 804–809.

[4] Mondal K, Nuñez L III, Downey CM, *et al.* Thermal barrier coatings overview: Design, manufacturing, and applications in high-temperature industries. *Ind Eng Chem Res* 2021, **60**: 6061–6077.

[5] Nair RB, Brabazon D. Calcia magnesia alumino silicate (CMAS) corrosion attack on thermally sprayed thermal barrier coatings: A comprehensive review. *NPJ Mater Degrad* 2024, **8**: 44.

[6] Ramirez Velasco JH, Kilaz G, Kenttämaa HI, *et al.* Application of biofuel impurities and effect on the hot corrosion of yttria-stabilized zirconia thermal barrier coatings. *Surf Coat Tech* 2019, **358**: 340–346.

[7] Guo L, Gao Y, Cheng YX, *et al.* Microstructure design of the laser glazed layer on thermal barrier coatings and its effect on the CMAS corrosion. *Corros Sci* 2021, **192**: 109847.

[8] Cheng B, Zhang X, Zheng GB, *et al.* Improving the CMAS corrosion resistance of $Gd_2Zr_2O_7$ TBCs via laser simultaneously induced texture/featherlike/dense structures. *J Mater Res Technol* 2025, **36**: 10104–10117.

[9] Zhang XF, Zhou KS, Xu W, *et al. In situ* synthesis of α-alumina layer on thermal barrier coating for protection against CMAS ($CaO–MgO–Al_2O_3–SiO_2$) corrosion. *Surf Coat Tech* 2015, **261**: 54–59.

[10] Zhuo XS, Sun XM, Wu J, *et al.* Molten CMAS resistance strategy for PS-PVD TBCs based on laser textured and Al-modified bionic structure. *NPJ Mater Degrad* 2024, **8**: 85.

[11] Zou LX, Gao MH, Xu N, *et al.* CMAS corrosion behavior of nanostructured YSZ and Gd–Yb–Y-stabilized zirconia coatings. *Coatings* 2023, **13**: 1623.

[12] Xiang Y, Yan K, Yu HY, *et al.* Comparative investigation on the hot corrosion failure of YSZ and GdYb-YSZ double-ceramic-layer thermal barrier coatings under $Na_2SO_4+V_2O_5$ molten salts. *Ceram Int* 2023, **49**: 18678–18688.

[13] Costa GCC, Acosta WA, Zhu D, *et al.* Thermochemistry of calcium–magnesium–aluminum–silicate (CMAS) and components of advanced thermal and environmental barrier coating systems Technical Report NASA/TM-2017-219512. Cleveland (OH): NASA Glenn Research Center, 2017.

[14] Schulz U, Braue W. Degradation of $La_2Zr_2O_7$ and other novel EB-PVD thermal barrier coatings by CMAS ($CaO–MgO–Al_2O_3–SiO_2$) and volcanic ash deposits. *Surf Coat Tech* 2013, **235**: 165–173.

[15] Chavez JJG, Naraparaju R, Mikulla C, *et al.* Comparative study of EB-PVD gadolinium–zirconate and yttria-rich zirconia coatings performance against Fe-containing calcium–magnesium–aluminosilicate (CMAS) infiltration. *Corros Sci* 2021, **190**: 109660.

[16] Zhang CG, Zhao JL, Yang L, *et al.* Preparation and corrosion resistance of nonstoichiometric lanthanum zirconate coatings. *J Eur Ceram Soc* 2020, **40**: 3122–3128.

[17] Guo L, Yan Z, Yu Y, *et al.* CMAS resistance characteristics of $LaPO_4$/YSZ thermal barrier coatings at 1250 °C–1350 °C. *Corros Sci* 2019, **154**: 111–122.

[18] Wang F, Guo L, Wang CM, *et al.* Calcium–magnesium-alumina–silicate (CMAS) resistance characteristics of $LnPO_4$ (Ln = Nd, Sm, Gd) thermal barrier oxides. *J Eur Ceram Soc* 2017, **37**: 289–296.

[19] Deng SX, He G, Yang ZC, *et al.* Calcium–magnesium–alumina–silicate (CMAS) resistant high entropy ceramic $(Y_{0.2}Gd_{0.2}Er_{0.2}Yb_{0.2}Lu_{0.2})_2Zr_2O_7$ for thermal barrier coatings. *J Mater Sci Technol* 2022, **107**: 259–265.

[20] Sun LC, Luo YX, Tian ZL, *et al.* High temperature corrosion of $(Er_{0.25}Tm_{0.25}Yb_{0.25}Lu_{0.25})_2Si_2O_7$ environmental barrier coating material subjected to water vapor and molten calcium–magnesium–aluminosilicate (CMAS). *Corros Sci* 2020, **175**: 108881.

[21] Sun YN, Xiang HM, Dai FZ, *et al.* Preparation and properties of CMAS resistant bixbyite structured high-entropy oxides RE_2O_3 (RE = Sm, Eu, Er, Lu, Y, and Yb): Promising environmental barrier coating materials for Al_2O_3f/Al_2O_3 composites. *J Adv Ceram* 2021, **10**: 596–613.

[22] Bahamirian M, Hadavi SMM, Farvizi M, *et al.* Microstructure and cyclic oxidation of yttria-stabilized zirconia/nanostructured ZrO_2–$9.5Y_2O_3$–$5.6Yb_2O_3$–$5.2Gd_2O_3$ thermal barrier coating at 1373 K. *J Mater Eng Perform* 2020, **29**: 7080–7093.

[23] Zhu DM, Chen YL, Miller RA. Defect clustering and nano-phase structure characterization of multi-component rare earth oxide doped zirconia-yttria thermal barrier coatings. In: Proceedings of the 27th Annual Cocoa Beach Conference on Advanced Ceramics and Composites: A: Ceramic Engineering and Science, 2008: 525–534.

[24] Wang TX, Shao F, Ni JX, *et al.* Calcium–magnesium–aluminum–silicate (CMAS) corrosion resistance of Y-Yb-Gd-stabilized zirconia thermal barrier coatings. *J Therm Spray Techn* 2021, **30**: 442–456.

[25] Song WJ, Yang SJ, Fukumoto M, *et al.* Impact interaction of in-flight high-energy molten volcanic ash droplets with jet engines. *Acta Mater* 2019, **171**: 119–131.

[26] Naraparaju R, Schulz U, Mechnich P, *et al.* Degradation study of 7 wt% yttria stabilised zirconia (7YSZ) thermal barrier coatings on

aero-engine combustion chamber parts due to infiltration by different CaO–MgO–Al_2O_3–SiO_2 variants. *Surf Coat Tech* 2014, **260**: 73–81.

[27] Wu Y, Song WJ, Dingwell DB, *et al.* Silicate ash-resistant novel thermal barrier coatings in gas turbines. *Corros Sci* 2022, **194**: 109929.

[28] Song WJ, Lavallée Y, Hess KU, *et al.* Volcanic ash melting under conditions relevant to ash turbine interactions. *Nat Commun* 2016, **7**: 10795.

[29] Xia J, Yang L, Wu RT, *et al.* Degradation mechanisms of air plasma sprayed free-standing yttria-stabilized zirconia thermal barrier coatings exposed to volcanic ash. *Appl Surf Sci* 2019, **481**: 860–871.

[30] Wu Y, Zhi WB, Li Y, *et al.* Interactions between rare-earth zirconates ($RE_2Zr_2O_7$) and CMAS silicate melts. *Corros Sci* 2023, **224**: 111526.

[31] Zan YX, Li CS, Yue PS, *et al.* Suppression of CMAS penetration by synergistic modulation of reaction-phase barrier in multi-rare-earth Co-doped zirconia. *Corros Sci* 2025, **254**: 113037.

[32] Liu G-L, Zhu L, Li X-Y, *et al.* Achieving durable double-layered thermal barrier coatings by tailoring multi-scale structures. *J Adv Ceram* 2024, **13**: 2068–2086.

[33] Jiang FR, Cheng LF, Wang YG. Hot corrosion of RE_2SiO_5 with different cation substitution under calcium–magnesium–aluminosilicate attack. *Ceram Int* 2017, **43**: 9019–9023.

[34] Tian ZL, Zhang J, Zheng LY, *et al.* General trend on the phase stability and corrosion resistance of rare earth monosilicates to molten calcium–magnesium–aluminosilicate at 1300 °C. *Corros Sci* 2019, **148**: 281–292.

[35] Li S, Chen WB, Zhao LD, *et al.* Calcia-magnesia-alumino-silicate-induced degradation of $(Gd_{0.9}Yb_{0.1})_2Zr_2O_7$ thermal barrier coatings prepared by plasma spray-physical vapor deposition (PS-PVD). *Surf Coat Tech* 2023, **454**: 129179.

[36] Bahamirian M, Hadavi SMM, Farvizi M, *et al.* Hot corrosion behavior of ZrO_2 $9.5Y_2O_3$ $5.6Yb_2O_3$ $5.2Gd_2O_3$ TBCs in CMAS: CaO–MgO–Al_2O_3–SiO_2. *J Aust Ceram Soc* 2021, **57**: 215–224.

[37] Jin XY, Huang YL, Peng F, *et al.* Research on the thermal properties and anti-CMAS performance of multi-component thermal barrier coatings. *NPJ Adv Manuf* 2025, **2**: 35.

[38] Gui C, Peng ZJ, Yao JT, *et al.* Improving corrosion resistance of rare earth zirconates to calcium–magnesium–alumina–silicate molten salt through high-entropy strategy. *Materials* 2024, **17**: 6254.

[39] Godbole E, von der Handt A, Poerschke D. Apatite and garnet stability in the Al–Ca–Mg–Si–(Gd/Y/Yb)–O systems and implications for T/EBC: CMAS reactions. *J Am Ceram Soc* 2022, **105**: 1596–1609.

[40] Holgate CS, Seward GGE, Ericks AR, *et al.* Dissolution and diffusion kinetics of yttria-stabilized zirconia into molten silicates. *J Eur Ceram Soc* 2021, **41**: 1984–1994.

[41] Krämer S, Yang J, Levi CG, *et al.* Thermochemical interaction of thermal barrier coatings with molten CaO–MgO–Al_2O_3–SiO_2(CMAS) deposits. *J Am Ceram Soc* 2006, **89**: 3167–3175.

[42] Zhang H, Chen Y, Li L, *et al.* Unraveling the CMAS corrosion mechanism of APS high-yttria-stabilized zirconia thermal barrier coatings. *J Eur Ceram Soc* 2024, **44**: 5154–5165.

[43] Mercer C, Faulhaber S, Evans AG, *et al.* A delamination mechanism for thermal barrier coatings subject to calcium–magnesium–alumino-silicate (CMAS) infiltration. *Acta Mater* 2005, **53**: 1029–1039.

[44] Sezavar A, Sajjadi SA, Babakhani A, *et al.* Thermal cyclic fatigue behavior of nanostructured YSZ/NiCrAlY compositionally graded thermal barrier coatings. *Oxid Met* 2019, **92**: 89–107.

[45] Shan X, Zou ZH, Gu LJ, *et al.* Buckling failure in air-plasma sprayed thermal barrier coatings induced by molten silicate attack. *Scripta Mater* 2016, **113**: 71–74.

[46] Tang ZY, Kotov NA, Magonov S, *et al.* Nanostructured artificial nacre. *Nat Mater* 2003, **2**: 413–418.

[47] Liu XJ, Li JL, Xiang L, *et al.* The role of matrix proteins in the control of nacreous layer deposition during pearl formation. *Proc Biol Sci* 2012, **279**: 1000–1007.

[48] Kakisawa H, Sumitomo T. The toughening mechanism of nacre and structural materials inspired by nacre. *Sci Technol Adv Mater* 2011, **12**: 064710.

[49] Wei ZY, Meng GH, Chen L, *et al.* Progress in ceramic materials and structure design toward advanced thermal barrier coatings. *J Adv Ceram* 2022, **11**: 985–1068.

[50] Cao XQ, Vassen R, Stoever D. Ceramic materials for thermal barrier coatings. *J Eur Ceram Soc* 2004, **24**: 1–10.

[51] Guo L, Li BW, Cheng YX, *et al.* Composition optimization, high-temperature stability, and thermal cycling performance of Sc-doped $Gd_2Zr_2O_7$ thermal barrier coatings: Theoretical and experimental studies. *J Adv Ceram* 2022, **11**: 454–469.

[52] Zou LX, Cheng YX, Meng SJ, *et al.* Construction of a molten CMAS-resistant bilayer-structured apatite layer used for thermal barrier coatings. *J Adv Ceram* 2025, **14**: 9221173.

[53] Jung M, Ji SG, Kim G, *et al.* Perovskite precursor solution chemistry: From fundamentals to photovoltaic applications. *Chem Soc Rev* 2019, **48**: 2011–2038.

[54] Li Y, Ding B, Chu QQ, *et al.* Ultra-high open-circuit voltage of perovskite solar cells induced by nucleation thermodynamics on rough substrates. *Sci Rep-UK* 2017, **7**: 46141.

[55] Shannon RD. Revised effective ionic radii and systematic studies of interatomic distances in halides and chalcogenides. *Acta Crystallogr A* 1976, **32**: 751–767.

[56] Van Orman JA, Grove TL, Shimizu N. Rare earth element diffusion in diopside: Influence of temperature, pressure, and ionic radius, and an elastic model for diffusion in silicates. *Contrib Mineral Petrol* 2001, **141**: 687–703.

[57] Leu LC, Thomas S, Sebastian MT, *et al.* Crystal structure of apatite type rare-earth silicate $(Sr_2RE_2)(RE_6)(SiO_4)_6O_2$ (RE = La, Pr, Tb, Tm, and Y). *J Am Ceram Soc* 2011, **94**: 2625–2632.

[58] Wu NN, Wang YL, Tong YL, *et al.* Interaction of ytterbium monosilicate environmental barrier coating material with molten calcium-magnesium-aluminosilicate (CMAS). *Corros Sci* 2023, **211**: 110864.